

# UC San Diego

## UC San Diego Previously Published Works

### Title

Laboratory evolution, transcriptomics, and modeling reveal mechanisms of paraquat tolerance.

### Permalink

<https://escholarship.org/uc/item/1150z65q>

### Journal

Cell Reports, 42(9)

### Authors

Rychel, Kevin  
Tan, Justin  
Patel, Arjun  
[et al.](#)

### Publication Date

2023-09-26

### DOI

10.1016/j.celrep.2023.113105

Peer reviewed



Published in final edited form as:

Cell Rep. 2023 September 26; 42(9): 113105. doi:10.1016/j.celrep.2023.113105.

## Laboratory evolution, transcriptomics, and modeling reveal mechanisms of paraquat tolerance

Kevin Rychel<sup>1</sup>, Justin Tan<sup>1</sup>, Arjun Patel<sup>1</sup>, Cameron Lamoureux<sup>1</sup>, Ying Hefner<sup>1</sup>, Richard Szubin<sup>1</sup>, Josefin Johnsen<sup>2</sup>, Elsayed Tharwat Tolba Mohamed<sup>2</sup>, Patrick V. Phaneuf<sup>2</sup>, Amitesh Anand<sup>3</sup>, Connor A. Olson<sup>1</sup>, Joon Ho Park<sup>4</sup>, Anand V. Sastry<sup>1</sup>, Laurence Yang<sup>5</sup>, Adam M. Feist<sup>1,2</sup>, Bernhard O. Palsson<sup>1,2,\*</sup>

<sup>1</sup>Department of Bioengineering, University of California, San Diego, La Jolla, CA 92093, USA

<sup>2</sup>Novo Nordisk Foundation Center for Biosustainability, Technical University of Denmark, Kemitorvet, Building 220, 2800 Kgs. Lyngby, Denmark

<sup>3</sup>Tata Institute of Fundamental Research, Homi Bhabha Road, Colaba, Mumbai, Maharashtra, IN

<sup>4</sup>Department of Chemical Engineering, Massachusetts Institute of Technology, 500 Main Street, Building 76, Cambridge, MA 02139, USA

<sup>5</sup>Department of Chemical Engineering, Queen's University, Kingston, ON K7L 3N6, Canada

### Summary

Relationships between the genome, transcriptome, and metabolome underlie all evolved phenotypes. However, it has proved difficult to elucidate these relationships because of the high number of variables measured. A recently developed data analytic method for characterizing the transcriptome can simplify interpretation by grouping genes into independently modulated sets (iModulons). Here, we demonstrate how iModulons reveal deep understanding of the effects of causal mutations and metabolic rewiring. We use adaptive laboratory evolution to generate *E. coli* strains that tolerate high levels of the redox cycling compound paraquat, which produces reactive oxygen species (ROS). We combine resequencing, iModulons, and metabolic models to elucidate six interacting stress tolerance mechanisms: 1) modification of transport, 2) activation of ROS stress responses, 3) use of ROS-sensitive iron regulation, 4) motility, 5) broad transcriptional reallocation toward growth, and 6) metabolic rewiring to decrease NADH production. This work thus demonstrates the power of iModulon knowledge-mapping for evolution analysis.

### Graphical Abstract

\*Corresponding author & lead contact: Bernhard O. Palsson, Correspondence: palsson@ucsd.edu.

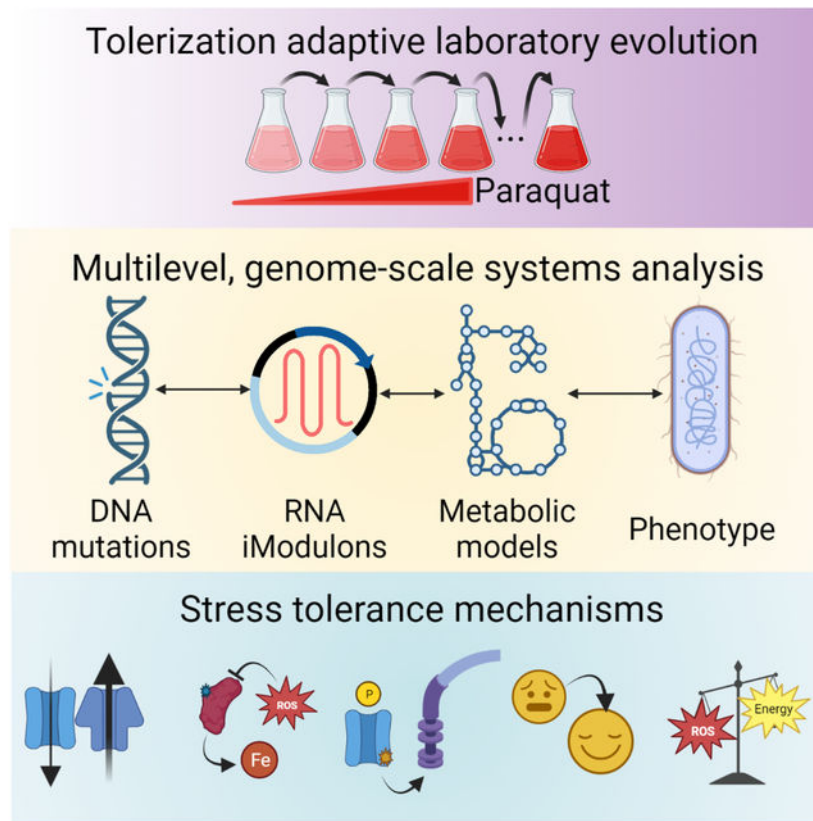
#### Author contributions

K.R., J.T., C.A.O., J.H.P., L.Y., A.M.F. and B.O.P. designed the study. J.T., J.H.P., R.S., Y.H., A.A., C.A.O., J.J., and E.T.T.M. performed experiments. K.R., J.T., A.V.S., P.V.P., and C.L. analyzed the data. A.P. performed simulations. K.R., J.T., and B.O.P. wrote the manuscript, with contributions from all the other co-authors.

**Publisher's Disclaimer:** This is a PDF file of an unedited manuscript that has been accepted for publication. As a service to our customers we are providing this early version of the manuscript. The manuscript will undergo copyediting, typesetting, and review of the resulting proof before it is published in its final form. Please note that during the production process errors may be discovered which could affect the content, and all legal disclaimers that apply to the journal pertain.

#### Declaration of interests

The authors declare no competing interests.



## eTOC

Adaptive laboratory evolution can reveal novel stress tolerance mechanisms, but typical methods struggle to interpret the rich information in transcriptomes of evolved strains. Rychel et al. evolved strains with high paraquat tolerance, and revealed six tolerance mechanisms by integrating iModulon-based transcriptomic analysis with other systems biology tools.

## Introduction

Adaptive laboratory evolution (ALE) is an excellent tool for discovery in biology. The experimental procedure is to grow a microbial starting strain in a selected condition for many generations, propagating when flasks reach a targeted density during repeated batch growth. This allows selection to enrich for mutant strains with improved fitness under the chosen condition<sup>6</sup>. A tolerization ALE uses this procedure with increasing stressor concentrations, pushing cells to amplify stress tolerance mechanisms<sup>7</sup>, thereby generating unique strains which are stress tolerance specialists. Analysis of ALE strains is highly informative for improving gene annotations, identifying fundamental biological principles and tradeoffs, designing bioproduction strains, and understanding antimicrobial resistance<sup>6,8,9</sup>.

Using ‘omics technology, we can globally characterize evolved strains from ALE studies. Typically, DNA resequencing and mutation calling algorithms<sup>8,10</sup> are used to enumerate all changes to the genome in each strain. Then, researchers perform a literature search

to map knowledge onto the mutated genes and make predictions about the mechanisms underlying the ALE. Researchers test those mechanisms with further experiments, and they employ a variety of other tools such as metabolic modeling<sup>2,3,11–15</sup> to discover new biological details about the strain and condition of interest. For example, Sandberg et al.<sup>16</sup> evolved *Escherichia coli* to grow well at elevated temperatures, and found genes that were consistently mutated in parallel. By relating these mutations to heat sensitive properties, the ALE analysis provides a clearer overall picture of the major weaknesses of the cell to heat stress. This understanding can then be applied for design of tolerant strains for bioproduction, and contribute to our understanding of the role of each gene in biological systems.

Several prior ALE studies have employed transcriptomics as part of the characterization tool kit. In principle, this data should be highly informative. Unlike the genome, the transcriptome is condition-specific. In addition, mutations can often have little or no effect<sup>17</sup>, but coordinated changes in gene expression often have a strong effect on phenotypes. However, the knowledge-mapping step, in which the transcriptome is mined for biological insights, is often challenging. The typical method for transcriptional analysis, differentially expressed gene (DEG) analysis, often returns a large number of DEGs, and determining their upstream regulation or downstream effects at large scales is daunting. We seek to integrate signals from the transcriptome with mutations in the genome via biologically meaningful relationships, which is difficult if we do not decrease the number of transcriptomic variables and map those variables to established knowledge from literature. This work would add global transcriptional analysis to the toolkit for understanding ALE strains.

iModulon analysis is a transcriptional analysis technique which has emerged as an effective way to reduce the number of transcriptomic variables and map knowledge onto them<sup>20,21</sup>. It uses independent component analysis (ICA) of large compendia of transcriptomic data to group genes into independently modulated sets (iModulons). iModulons are comparable to regulons. Regulons are the sets of genes that respond to a particular regulator as determined by bottom-up methods such as chromatin immunoprecipitation and regulator knock-outs<sup>18,19</sup>, whereas iModulons are determined from the top-down by analyzing only trends in transcriptomes. iModulons are therefore more flexible, and can capture the effects of regulatory changes along with other signals, like genomic deletions. They are also more amenable to computation: they are based on matrix decomposition, and each iModulon has an activity level in each sample, which can be combined with gene weightings to calculate the expression of the set of genes. By comparing iModulons with regulon annotations<sup>22</sup>, each iModulon is manually curated with predicted regulators and functions, bridging between the statistical patterns in data and existing literature. iModulon activity levels can be used to infer the activity of their underlying regulators, and thus enable quantitative interrogation of the cell's sensory systems. This approach has provided valuable insights into *E. coli*<sup>20,23</sup> and several other organisms<sup>24–31</sup>. iModulon analysis is supported by a publicly available codebase and online knowledgebase ([iModulonDB.org](http://iModulonDB.org))<sup>21,32</sup>.

We have recently updated our iModulon structure for *E. coli* using a dataset with over 1,000 samples, called PRECISE-1K<sup>23</sup>. Data from the present study was included in this

dataset, which computed and characterized 201 signals in the transcriptional regulatory network (TRN) and reported details on [iModulonDB.org](https://iModulonDB.org). In this study, we demonstrate the usefulness of this knowledge-enriched representation by iteratively characterizing each significant transcriptional signal (iModulon) that changed over the course of an ALE. We identify relationships between mutations, iModulons, the ALE condition, and other results such as physiological measurements and metabolic models. Though iModulons have been used in past ALE studies<sup>11,12,33–35</sup>, no other study has iterated through each significant signal in the transcriptome in a way that mirrors the iterative interpretation of each mutation. Inference from the transcriptome reveals a large set of phenotypic predictions, many of which are more complex than would be identifiable by previous methods. This motivates further use of the iModulon framework as an important new part of the ALE analysis toolkit.

We used ALE to generate *E. coli* strains which are specialized to tolerate a common herbicide, the redox cycling compound paraquat (PQ). Redox cycling compounds generate large amounts of reactive oxygen species (ROS) by stripping electrons from cellular electron carriers, such as NADH and NADPH, and reducing oxygen; this generates destructive superoxide ROS and regenerates the oxidizing agent to re-initiate the cycle<sup>36–38</sup>. The ROS are particularly damaging to iron-containing enzymes and DNA. They decrease activity of important pathways, challenge the integrity of the genome, and inhibit growth<sup>3,37,39–42</sup>.

Though the ROS response of *E. coli* is well understood and ROS are often delivered in the laboratory by PQ<sup>40</sup>, some questions remain about how high levels of tolerance can be achieved: (i) In addition to the known proteins, which transporters and enzymes are involved in PQ cycling? (ii) What transcriptional alterations, specifically with respect to stress responses, metal homeostasis, and redox balance, are optimal? (iii) How can cells balance a tradeoff between generating NAD(P)H for energy and decreasing its production to prevent redox cycling<sup>36–38</sup>? Through our unique combination of systems biology techniques and new emphasis on iModulon knowledge-mapping, we are able to shed new light on these questions. Their answers are informative for the fundamental biology of stress and metabolism, and for applications in pathology, antimicrobial design, and biomanufacturing.

This work provides a blueprint for combining iModulon analysis with ALE. We begin by characterizing the strains and presenting an overview of the genomic and transcriptional changes. We then show the effects of large DNA changes and TF mutations on the transcriptome. We also find an unexpected non-TF mutation that regulates motility regulons in our strains. Next, we disentangle the large fraction of the transcriptome which responds to changes in stress and growth phenotypes. Finally, we propose and model a metabolic mechanism for PQ tolerance involving several mutations and broad transcriptional reallocation. We show that the evolved strains employ a multi-pronged strategy of: (i) modifying membrane transport, (ii) using the SoxS and OxyR regulons to ensure stress readiness, (iii) allowing ROS-sensitive iron-sulfur (Fe-S) clusters to play a larger role in regulation of metal homeostasis, (iv) increasing motility, (v) shifting transcriptional allocation toward growth, and (vi) using fermentation to avert the PQ cycle.

## Results

### Laboratory evolution increased tolerated PQ levels by 1000%

We evolved strains aerobically in minimal media with glucose under increasing PQ stress (Figure 1A). Our starting strain (0\_0) was a derivative of *E. coli* K-12 MG1655 which had been pre-evolved to grow in minimal media with glucose<sup>43</sup>. By using this media-adapted starting strain, the subsequent ALEs were enriched for mutations which improve stress tolerance, since the mutations that promote rapid growth under the culture conditions were already fixed (Table S1). ALE was performed by steadily increasing PQ concentrations, first in three parallel first generation ALEs (1\_0, 2\_0, 3\_0) and followed by eleven second generation ALEs (1\_1, 1\_2, ..., 2\_1, etc.) (Figure 1A–B). Parallelizing ALE replicates generated diverse strains and allowed for identification of common mutation targets which are more likely to be causal.

After evolution, growth rates for each endpoint under different PQ concentrations were measured (Figure 1C). The starting strain's growth was severely impaired by low PQ concentrations, with no growth at 250  $\mu$ M PQ. The evolved strains showed a dramatic increase in the concentration of PQ they can tolerate while still growing; some endpoint strains tolerated 2500  $\mu$ M. There was a fitness cost to the PQ tolerance, however: the strains no longer grew as well in the absence of PQ as the starting strain. This observation is consistent with the tradeoffs of the PQ tolerization mechanisms.

### Adaptive mutations reflect effects of PQ

Across the entire set of evolved endpoint strains in the PQ ALE, a total of 222 mutations were observed, representing 111 unique sequence changes. These totals include point mutations, indels, and amplifications as determined by the mutation caller. Each mutation was assigned to its closest gene in the case of intergenic mutations, and 72 total genes were affected. No new mutations in the previously mutated genes were observed, and none of the mutations reverted. Mutations were then categorized by their likely effects and visualized in a treemap where larger areas indicate genes that were more commonly mutated in the endpoint strains (Figure 1D, Table S2). The largest category of mutated genes was central and energy metabolism-related (35%), which reflect the metabolic effects of PQ on redox balance. Transporters were also frequently mutated (16%), likely to prevent influx or promote efflux of PQ or other ROS. Iron and iron-sulfur (Fe-S) clusters are sensitive to oxidative stress<sup>40</sup>, so we observed changes to iron regulators and Fe-S cluster synthesis genes (16%). Three large deletions were also notable (5%). Other mutations which were less convergent across endpoint strains (26%) were observed in ribosomal subunits, tRNAs, and *lon* protease, as well as across other parts of the metabolic network.

We performed DNA sequencing on several midpoint strains during the ALEs (Figure 1B), which provided insight into the most effective growth strategies since mutations tend to fix in the order of fitness benefit<sup>44</sup>. We note that *emrE* and *aceE* are among the first genes to be affected in all three of our first generation strains.

An interesting pattern arose in the observed single nucleotide polymorphisms (SNPs): compared to other ALE projects available on ALEdb<sup>8</sup>, they are highly enriched for changes

from guanine or cytosine to adenine or thymine (Figure 1E; Fisher's exact test  $p = 9.38 \times 10^{-5}$ ). This enrichment was consistent with direct damage to DNA by ROS, since guanine is the most easily oxidized nucleotide<sup>39,45,46</sup>. Thus, these mutations might not only improve cellular fitness through genomic and transcriptomic changes, but also by physically tolerizing cellular DNA to oxidation.

### **iModulons enable analysis of complex transcriptomic changes**

To identify transcriptomic adaptations, we performed RNAseq on the starting strain at 0 and 250  $\mu\text{M}$  PQ, and on each evolved strain at 0, 250, and 750  $\mu\text{M}$  PQ. In a comparison between the stressed samples for the pool of all evolved strains vs. the starting strain, we found 1,774 differentially expressed genes (DEGs) (Figure 1F), making detailed analysis using traditional transcriptomic methods challenging. Therefore, we applied iModulon analysis to enable interpretation.

The data was previously included in a large compendium of *E. coli* RNAseq data generated from a single wet lab protocol (PRECISE-1K<sup>23</sup>). By leveraging over 1,000 samples across diverse conditions, this dataset facilitated machine learning of global transcriptomic patterns. Following our pipeline<sup>32</sup>, ICA was performed on the full dataset. The result was a set of 201 iModulons, independently modulated gene sets which have similar expression patterns, along with their activities in each sample. iModulons reflect signals of any source that may affect the transcriptome: 'Regulatory iModulons' are those that are likely regulated by a known regulator, 'Biological iModulons' are enriched for a biological function but no currently known regulator, 'Genomic iModulons' represent the transcriptomic effect of changes to the genome in some samples in the data, and 'Uncharacterized iModulons' may be the result of technical noise or other unknown signals<sup>20</sup>. Together, the iModulons constitute a quantitative regulatory structure which maps well to the known TRN, and can be used to reduce the dimensionality of the dataset. The set of PRECISE-1K iModulons was characterized in a separate study<sup>47</sup>, and the iModulon structure is available at [iModulonDB.org](https://iModulonDB.org) under *E. coli* PRECISE-1K<sup>21</sup>. In the remainder of this paper, we show the usefulness of applying the iModulon knowledge-mapping performed in the previous study to gain detailed biological insights as part of an ALE analysis toolkit.

iModulons enabled a global characterization of changes in the transcriptome. They summarize expression of sets of genes in an activity level, where each gene is weighted based on the strength of its predicted association with the regulatory signal. The evolved strains' gene expression under PQ stress against the starting strain had only 42 statistically significant differential iModulon activities (DiMAs) (Figure 1G). Compared to the hundreds of DEGs, these 42 iModulon changes made the analysis of the large-scale changes in the transcriptome tractable. We iteratively characterized and categorized each of the DiMAs and assigned mechanistic hypotheses which explain their changes (Table S3). We also summarized the explained variance in the transcriptome (Methods) in Figure 1H, where the transcriptome is first broken into significant iModulon signals that exhibit a change after ALE, insignificant iModulon changes, and variance not captured by the iModulon structure. The significant iModulon signals are further broken down into categories, where stress-related and metabolic signals reflect the largest changes in the data.

## Mapping between the genome and transcriptome reveals new insights

Modifications to the genome can affect the transcriptome in several ways: large deletions and duplications can directly alter the expression of genes involved, mutations in TFs can change the expression of their associated regulons, and the transcriptome can adjust due to changes in metabolites or other sensed processes that result from mutations. The latter type of alteration can be complicated by the fact that gene expression also regulates metabolite concentrations and sensed processes. In Figure 2A, we summarize how each of these types of relationships were observed in the evolved strains. Each relationship depicted in the figure was associated with evidence from our data and the literature, and several relationships are new; we provide all details in Table S4. iModulons play a central role in each highlighted mechanism, as evidenced by the full second column in Figure 2A. The combined analysis of genomic and transcriptional changes led us to six key cellular mechanisms of PQ tolerance (Figure 2B). We will now describe each of these relationships in order of increasing complexity.

### Large amplifications and deletions in the genome affect membrane transport

‘Genomic iModulons’ are transcriptomic modules which capture the effect of large changes to the genome, so they are of primary interest for obtaining genome-to-transcriptome relationships. In the PQ tolerant strains, the major genomic iModulons happen to all be associated with alterations in membrane transport.

The first mutation in each of the first-generation strains affected *emrE*, a multidrug efflux pump which pumps out PQ<sup>48</sup>. In 1\_0, 2\_0, and their subsequent evolutions, DNA sequencing reads mapped increased approximately 42-fold in the region containing *emrE* (Figure 3A). This was likely caused by repeated duplication (amplification) which may have been mediated by the flanking DLP12 prophage insertion sequence (IS) genes, specifically the IS3 transposase elements *insEF3*<sup>49</sup>. ICA of the transcriptome recovered the amplified genes as an independent signal in the dataset, which we named the *emrE* Amp iModulon (called ROS TALE Amp-1 in PRECISE-1K<sup>23</sup> on [iModulonDB.org](http://iModulonDB.org)<sup>21</sup>). This iModulon showed elevated activity levels in all affected strains regardless of PQ concentration (Figure 3C). Thus, this case illustrates a relationship between the genome (gene amplification) and transcriptome (*emrE* Amp iModulon) with a likely beneficial phenotype (PQ efflux) – knowledge-mapping between these three levels to generate hypotheses like this one is the goal of our new approach (Figure 2A).

We discuss Del-1, and Del-2, large deletions that contain several transporters (Figure 3B, D, E), and additional transporter mutations of potential interest (Figure 3F) in Supplementary Data S1 – Note S1. We hypothesize that these mutations and their related genomic iModulons may have decreased influx of PQ or other oxidized molecules.

### Mutations in TFs alter the regulation of stress responses and iron homeostasis

‘Regulatory iModulons’ are iModulons which are statistically enriched with genes from a specific regulon, and their activity level quantifies the activity of the underlying TF. Thus, iModulon analysis reveals the effects of TF mutations in a convenient way.



The OxyR iModulon contains oxidative stress response genes, and its regulator, OxyR, responds to oxidative stress<sup>50</sup>. Thus, we expected its activity level to correlate with PQ level. We found that for most strains, this is the case (Pearson;  $p = 6.2 \times 10^{-5}$ ). However, we observed three separate *oxyR* mutations which all fix OxyR iModulon activity levels at a level just below that of the stressed starting strain (Figure 4A), regardless of PQ concentration. We speculate that this level may be ideal because it enables quick detoxification of ROS, while higher levels would be proteomically expensive and/or induce growth-limiting levels of *oxyS* (which is regulated by OxyR and leads to growth arrest<sup>51</sup>). Previous iModulon work in other ALEs found that fixing OxyR in the active conformation provided a fitness benefit<sup>35</sup>. Without the OxyR iModulon to quantify OxyR activity, it would have been much more difficult to define the effect of these mutations.

Fur, the ferric uptake regulator, regulates two main iModulons (Fur-1 and Fur-2) whose activities have a nonlinear relationship<sup>52</sup> (Figure 4B–D, S1A). Three separate strains acquired *fur*P18T, which appears to shift Fur's preference above the trend line, towards Fur-2 (Figure 4E). They specifically upregulate the expression of *feoABC*, a ROS-sensitive iron transporter<sup>53</sup> (Figure 4F). By using *feoABC* to strongly couple iron uptake to ROS levels, this mutation should prevent ROS-induced iron toxicity by preventing iron uptake under high stress (Supplementary Data S1 – Note S2; Figure 4G). This mutation is of interest for further study, since it modifies the TRN in a unique way, and promotes a strategy of ROS-sensitive iron uptake that may be useful for production strains that are hampered by ROS.

The TFs IscR and SoxS also provide important insights (Figure S1; Supplementary Data S1 – Note S3).

These results highlight the efficacy of iModulon analysis for revealing TF mutational mechanisms. The Fur and IscR mechanisms predict that the ROS-sensitivity of Fe-S clusters can be used to couple iron uptake or utilization to ROS levels. The particular mutations ought to be introduced into production strains, where they could increase yields if ROS stresses are limiting.

### An unexpected mutation in *pitA* upregulates motility

A frameshift in the phosphate transporter *pitA* led to a motile phenotype. This mutation occurred in 1\_0 and its derivatives, and these strains also exhibited strong activation of motility-associated iModulons such as FliA (Figure 4H). There is no obvious connection between phosphate transport and motility, and the mutated strains were likely able to use the other phosphate transport system, *pstABCS*, to meet their phosphorus needs<sup>54</sup>. Interestingly, the 3\_0 strain deleted *pitA* as part of Del-1 (Figure 3B), and it did not exhibit the motility phenotype. Thus, to understand this mutation, we generated two new strains: 0\_0::*pitA*\* and 1\_0::*pitA*, which added the mutation on its own to the starting strain and removed it in favor of the original *pitA* sequence in the evolved strain, respectively. We found that the mutation provided a growth advantage under PQ stress (Figure 4I). We also transcriptomically profiled the strains under the same conditions used for our other strains, and found that, particularly under PQ stress, the mutation exclusively perturbs the motility iModulons (Figure 4J). The change to the transcriptome was also reflected in the

phenotype, as the mutant strains swarmed on agar plates while the wild-type *pitA* strains did not (Figure 4K, S2). The detailed mechanism of action linking the *pitA* mutant to motility remains to be elucidated. There is also a possible connection to fermentation<sup>55</sup> (Figure S2A, Supplementary Data S1 – Note S4).

This section illustrates the usefulness of our multilevel approach. After connecting mutations to their effects and predicting causes for DiMAs, we were left with an orphan mutation (*pitA*) and an unexplained DiMA (FliA). We predicted that the mutation caused the DiMA, and then we generated new strains to validate the prediction. The recapitulation of the expected iModulon change and swarming phenotype lends credibility to the iModulon method of elucidating mutational effects.

### Shifting from stress to growth explains activity of several iModulons

Regulatory iModulons can be used not only to understand the direct effects of mutations as described above, but also effects of changes to the processes that TFs sense. We have divided these types of changes in the PQ tolerant strains into two categories: those that respond to stress and growth (21% of the variance in the transcriptome; Figure 1H), and metabolic changes (10%). In this section we describe the former.

An important global tradeoff in the *E. coli* transcriptome is between growth and general stress readiness, which is governed by complex regulation<sup>56,57</sup>. We previously described a ‘fear-greed tradeoff’ between the RpoS and Translation iModulons, in which the activity levels of the two iModulons have a negative correlation; faster growing cells exhibit low RpoS and high Translation activity<sup>20,35,52,58–60</sup>. Mutations which downregulate the RpoS regulon have been known to increase growth in long term culture<sup>61</sup>. A similar tradeoff between stress readiness and nutritional competence has also been described<sup>62</sup>. This previous knowledge can be applied to the new ALE strains: the starting strain without stress is ‘greedy’, but it becomes ‘fearful’ upon addition of PQ, as expected (Figure 5A–B). The evolved strains, on the other hand, largely remain ‘greedy’ in the presence of PQ; they strongly downregulate RpoS (Figure 5A) and have higher translation activity than the stressed starting strain (Figure 5B). Translation activity is decreased relative to the starting strain in the absence of PQ, likely because of tradeoffs towards ROS stress readiness.

Despite the presence of stressors and the activation of specific ROS responses OxyR and SoxS, the general stress response is not activated in the evolved strains. The stress signals are downregulated by the success of the evolved tolerance strategies, and the growth-inhibiting effects of RpoS have selected against strains with high RpoS activity. This work agrees with previous findings that ALE shifts allocation toward ‘greed’<sup>20,35,58</sup>. The decoupling of the ROS and general stress responses makes these strains ROS-response specialists, constituting a valuable adaptation strategy.

Two DiMAs reflect a decrease in oxidative damage by sensing Fe-S-dependent metabolites. The Leucine iModulon (Figure 5D) encodes the leucine biosynthesis pathway, which requires an Fe-S cluster and other metal-dependent enzymes that are sensitive to oxidative stress<sup>63</sup>. Leucine feeds back to inhibit the iModulon’s expression<sup>64</sup>. In the starting strain with PQ, oxidative damage likely leads to a decrease in leucine concentrations and an

upregulation of the iModulon. By contrast, the evolved strains experience less stress, protect their Fe-S clusters, and therefore exhibit low Leucine iModulon activity. Similarly, the Biotin iModulon (Figure 5E) uses an Fe-S cluster in BioB to synthesize biotin<sup>65</sup>, which then controls iModulon activity via regulation by BirA<sup>66</sup>.

The activities of the ppGpp, Purine, Ribose, Cysteine-1, and Copper iModulons (Figure 5C, F–I) each also reflect decreased stress and a return to homeostasis in the evolved strains (Figure 5J; Supplementary Data S1 – Note S5).

Thus, iModulons measure the sensory output of the TRN and allow us to mine the transcriptome for insights into many cellular processes. Because we also have an understanding of the stress phenotype of our cells, we predicted reasons for a large fraction of transcriptional alterations. This approach would be useful to any researcher seeking to enumerate phenotypic alterations in novel strains using RNAseq data as a guide.

### Mutating central and energy metabolism genes decreases PQ cycling

We now turn to metabolism, which involves a complex interplay of effects (Figure 2A). We show that enzyme mutations can suggest tolerance strategies, and then modeling can validate them. iModulon analysis reveals how those strategies are organized and regulated by the cell.

The main metabolic mutations occur in the tricarboxylic acid (TCA) cycle. The second gene to mutate in all strains was *aceE* (Figure 1B, D). *aceE* encodes a subunit of pyruvate dehydrogenase (PDH), the entry point into the TCA cycle. *gltA*, *sucA*, and *icd* also mutate often, with *icd* being affected by e14 deletion and SNPs<sup>68</sup> (Figure 6A). These mutations would likely decrease the function of the enzymes, thus decreasing TCA cycle flux and production of NADH. These mutations suggest a tolerance benefit to decreasing NADH production. The likely reason for this benefit is that PQ uses electrons from NAD(P)H to reduce oxygen and generate stress<sup>69–71</sup>. These mutations decrease the available electrons to the PQ cycle and prevent stress generation. To decrease oxidative stress from PQ, the evolved strains perform less oxidative metabolism. The supplementary Fe-S and motility mechanisms (Supplementary Data S1 – Note S3, S4) also shift strains away from NADH production.

Loss of function (LOF) mutations in the TCA cycle come with a cost, since those pathways are the primary energy source for aerobic cells. Indeed, the evolved strains have decreased growth and translational activity under no stress relative to the starting strain, probably for this reason (Figure 1C, 5B). During ALE, the strains must therefore balance a tradeoff: generate enough NADH to grow and repair themselves, but not so much as to over-empower the PQ cycle. The tradeoff is embodied by an interesting interaction between mutations the *aceE* and *glnX* mutations, in which a tRNA mutation partially restored PDH activity (Figure 6B; Supplementary Data S1 – Note S6).

We summarize all metabolic mutations in Figure S3 and Table S2. We also observe mutations in enzymes involved in the utilization of NADH (Figure S3A; Supplementary

Data S1 – Note S7). Next, we characterize the strains using a variety of tools to test this explanation for the selection for TCA cycle mutations.

### Metabolic rewiring towards a lower aero-type decreases PQ sensitivity and flux in evolved strains

We quantified glucose uptake for each strain at various PQ levels (Supplementary Data S1 – Note S8), and generated a plot comparing biomass yield per gram of glucose to the glucose uptake rate (Figure 6C). This rate-yield plane has been characterized in past studies<sup>12,67</sup>, which revealed distinct energy generation strategies (aero-types) for each position in the plane. Samples with high biomass yields are in the highest aero-type (aero-type  $\nu$ ), which represents efficient aerobic growth, whereas lower aero-types are associated with lower aerobicity and secretion of organic acids<sup>12</sup>.

In Figure 6C, we observe a switch to a lower aero-type in the starting strain upon PQ exposure, since ROS damage decreases growth rate and particularly damages respiration. In the evolved strains, the lower aero-type is maintained even when no PQ is present. The aero-type change is likely due to the TCA cycle-related mutations, which we predicted would decrease respiration. However, the evolved samples also shift rightward, increasing their glucose uptake and total metabolic flux, enabling them to maintain growth under stress. Their position in the plane doesn't vary much with PQ concentration, indicating decreased sensitivity.

To characterize metabolism *in silico*, we used OxidizeME, a genome-scale computational model of *E. coli* metabolism and expression (ME) which incorporates ROS stress effects<sup>3</sup>. We constrained the model using growth rates, glucose uptake rates, and RNA expression, then simulated optimal steady states (Figure 6D, S4). Though we did not attempt to simulate the effects of mutations on the reaction rates, the optimal flux distributions in the evolved strains showed decreases in TCA cycle flux (Figure 6E), consistent with the predicted effects of the mutations.

In the absence of experimental methods for directly measuring PQ cycle flux, we computationally assessed the consequences of PQ cycle flux by varying it for the starting strain and a representative evolved strain (Figure 6F–G). Though total proteomic allocation to the TCA cycle was constrained to match the RNA expression, ROS damage to the Fe-S clusters in *acnA*, *fumAB*, and *sdhABCD* led to decreasing functional proteome fractions (Figure 6F). The starting strain relied more heavily on the TCA cycle; this made it more sensitive to PQ, as evidenced by the steeper slope in NADH production (Figure 6G). The starting strain was also able to grow at higher PQ fluxes, which is inefficient and exacerbates stress. Thus, tolerization both decreases sensitivity to lower PQ fluxes and prevents a steady state with high PQ flux.

The genome-scale OxidizeME model integrates the individual cellular processes and RNA expression changes which adjust the phenotype, and it elucidates key systems level tolerization strategies. Its results match expectations from mutational analysis.

## iModulon activities shift tolerant strains towards anaerobic metabolism and glycolysis

Finally, we discuss iModulons which regulate the metabolic rerouting presented above. The cellular oxidation state is sensed and regulated by ArcA and Fnr<sup>72</sup>, whose iModulons are differentially activated in the evolved strains (Figure 7A–D). Both TFs sense redox balance, which shifts towards reduction in the evolved strains due to the successful tolerization: ArcA represses when the electron transport chain is in a reduced state<sup>73</sup>, whereas Fnr repression ceases when Fe-S clusters are intact<sup>74</sup> (Figure 7E). These transcriptional changes shift from aerobic respiration genes toward anaerobic fermentation genes<sup>72</sup> (despite the aerobic ALE conditions). This strategy maintains a lower aero-type and decreases reliance on NADH. Thus, this mechanism reinforces the decreased reliance on the TCA cycle brought on by the mutations, ultimately slowing PQ cycling.

To meet energy needs with lower respiration, the cells increased their glycolytic activity, a change which is described by two DiMAs. Cra iModulon activity increases, indicating an increase in glycolytic flux (Figure 7F). Similarly, the Crp-2 iModulon returns to unstressed or intermediate levels in the evolved strains, which indicates a more active phosphotransfer system (Figure 7G). This transcriptomic change matches the rightward shift in the aero-type plot (Figure 6C). Finally, the LOF mutations downstream of pyruvate should increase pyruvate concentrations, which strongly upregulate the Pyruvate-2 iModulon (Figure 7H). More details for all transcriptional mechanisms in this section are provided (Supplementary Data S1 – Note S9).

In the past three sections, we showed that mutations and iModulon activity adjustments work together to enforce a low aero-type, PQ-tolerant metabolic network. The PQ tolerance stems from a decreased reliance on the TCA cycle and decreased NADH production, which leads to less total PQ cycling and makes the system less sensitive to small amounts of PQ cycling. It is often difficult to interpret biological systems when genes, gene expression, and metabolic flux are all changing, but our multilevel approach produced a consistent and comprehensive interpretation of multiple data types.

## Discussion

We combined ALE with a detailed, systems-level transcriptomic analysis to reveal mechanisms underlying PQ tolerance. The approach spanned four ALE analysis tools (Figure 2A): (i) genetic alterations and their predicted effects, (ii) transcriptomic adaptations along with up- and downstream inferences about their regulatory causes and physiological impact, (iii) metabolic fluxes calculated from genome-scale metabolic models, and (iv) phenotypic changes such as swarming motility. We found iModulon analysis to be particularly revealing, as the TF activities could be readily quantified and utilized to infer a wealth of information about the phenotypic state. We combined these approaches to summarize a coherent set of PQ tolerization strategies.

The evolved strains achieved high tolerance through several mechanisms (Figure 2B). They promoted efflux of PQ via *emrE* segmental amplification, and precluded influx by mutating or deleting various other transporters. Inside the cells, PQ failed to generate as much ROS due to LOF mutations in and downregulation of NADH-producing pathways. To compensate

for the decreased biomass yield of their metabolism, the cells increased glucose uptake and glycolytic flux. Since ROS interact with iron, some strains modified iron regulation via TF mutations that curtailed these systems when stress was high. These mutational and metabolic strategies led to a decrease in stress, which was sensed by the TRN and shifted various regulators toward faster growth.

The impact of this study is threefold. (i) We present biological insights of wide interest to researchers, including the growth/stress tradeoff of redox metabolism, the use of Fe-S clusters as a brake on iron uptake and metabolism, and novel interactions such as those between *pitaA* and motility and between *aceE* and *glnX*. (ii) Acquired mutations and iModulon activities can become design variables to mitigate oxidative stress for bioproduction applications. (iii) We demonstrate an approach that utilizes iModulons to reveal a novel integrated perspective on adaptation to stress by understanding transcriptomic allocation.

Taken together, our results demonstrate the usefulness of curated iModulon structures like PRECISE-1K as part of the hypothesis-generation toolkit for ALE strain analysis. We elucidate several systems-level strategies of ROS tolerization using genome-scale datasets, computational models, and detailed literature review. Given the falling cost of RNAseq, development of laboratory evolution, and the availability of this pipeline developed here, we expect that future ALE-derived and other strains can also be characterized from this new perspective, revealing novel cellular functions and adaptations.

### Limitations of the study

The application of iModulon analysis to ALE as performed here has important limitations to note. Firstly, iModulons are not a perfect representation of the transcriptome: as described in other publications<sup>20,23</sup>, the ICA algorithm assumes that each regulator behaves independently, has a non-gaussian activity distribution in the dataset, and has a linear effect on genes. These assumptions enable a quantitative representation that is better than competing algorithms<sup>75</sup>, but may break down for the more complex regulons. Also, as with any dimensionality reduction, not all variance in expression is captured by the iModulons: in the samples discussed here, the iModulons explain 80.5% of the original expression dataset. In addition, the regulator annotations for each iModulon are statistically significant, but they may not accurately capture all of the regulation underlying each set of genes. For this reason, the more complicated observations were double-checked against the original data matrix, and we do not claim to mechanistically explain the entire transcriptome.

Another key limitation of the study is that the relationships put forward have not been rigorously tested. The scope of this work is to demonstrate how knowledge-mapping from major signals of the transcriptome leads to mechanistic predictions about a wide variety of systems in ALE. This gives this manuscript a broad scope, and we strongly encourage follow-up studies to rigorously test specific hypotheses. We clearly state the available evidence in the manuscript, supplemental notes, and Table S4.

## STAR Methods

### Resource Availability

**Lead contact**—Further information and requests for resources and reagents should be directed to and will be fulfilled by the lead contact, Bernhard Palsson (palsson@ucsd.edu).

**Materials availability**—Strains generated in this study are available upon request.

**Data and code availability**—RNA-seq data have been deposited to GEO and are publicly available as of the date of publication, under accession numbers GSE134256 and GSE221314. DNA-seq data are available from [aledb.org](http://aledb.org) under the project “ROS”. iModulons and related data are available from [iModulonDB.org](http://iModulonDB.org) under the dataset “*E. coli* PRECISE-1K”.

All original code and data to generate figures are available at [github.com/SBRG/ROS-ALE](https://github.com/SBRG/ROS-ALE), which also links to the alignment, ICA, and iModulon analysis workflows<sup>32</sup>. It has been deposited at Zenodo and is publicly available as of the date of publication<sup>76</sup>. The DOI is [10.5281/zenodo.7449004](https://doi.org/10.5281/zenodo.7449004).

Any additional information required to reanalyze the data reported in this paper is available from the lead contact upon request.

### Experimental Model and Subject Details

**Microbial strains**—The starting strain (0\_0) was an MG1655 K-12 *E. coli* strain which had been evolved for optimal growth on glucose as a carbon source in M9 minimal media<sup>43</sup>. Mutations for the starting strain are given in Table S1, and mutations for all strains are listed on [aledb.org](http://aledb.org) and in Table S2.

**Culture conditions**—Strains were grown overnight in M9 minimal media with 0.4% w/v glucose as a carbon source. Fresh media was inoculated with the overnight culture at an initial 600 nm optical density (OD) of 0.025. Cultures were aerated with a stir bar at 1100 rpm in a water bath maintained at 37°C until OD reached 0.5. 50 mM PQ was added to reach the desired concentration in stressed flasks. After 20 minutes, samples were harvested for transcriptomics or ribosome profiling.

### Method Details

**Adaptive laboratory evolution**—ALE was performed using a similar protocol to Mohamad *et al.* 2017<sup>77</sup>. Parallel cultures were started in M9 minimal medium by inoculation from isolated colonies. Evolution was performed in an automated platform with 15 mL working volume aerobic cultures maintained at 37°C and magnetically stirred at 1100 rpm. Growth was monitored by periodic measurement of the 600 nm OD on a Tecan Sunrise microplate reader, and cultures were passaged to fresh medium during exponential cell growth at an OD of approximately 0.3. Growth rates were determined for each batch by linear regression of ln(OD) versus time. At the time of passage, PQ concentration in the fresh medium batch was automatically increased if a growth rate of 0.08 h<sup>-1</sup> had been met

for 3 consecutive flasks. Samples were saved throughout the experiment by mixing equal parts culture and 50% v/v glycerol and storing at  $-80^{\circ}\text{C}$ .

**DNA sequencing and mutation calling**—DNA was isolated as described<sup>78</sup>. Total DNA was sampled from an overnight culture and immediately centrifuged for 5 min at 8,000 rpm. The supernatant was decanted, and the cell pellet was frozen at  $-80^{\circ}\text{C}$ . Genomic DNA was isolated using a Quick-DNA Fungal/Bacterial Microprep Kit (Zymo Research) following the manufacturer's protocol, including treatment with RNase A. Resequencing libraries were prepared using a Kapa Hyper Plus Kit (Roche Diagnostics) following the manufacturer's protocol. Libraries were run on HiSeq and/or NextSeq (Illumina).

Sequencing reads were filtered and trimmed using AfterQC version 0.9.7<sup>79</sup>. We mapped reads to the *E. coli* K-12 MG1655 reference genome (NC\_00913.3) using the breseq pipeline version 0.33.1<sup>10</sup>. Mutation analysis was performed using ALEdb<sup>8</sup>.

**Physiological characterization**—Growth curves and extracellular glucose and organic acid concentrations were obtained by inoculating cells from an overnight culture to a low OD using the same conditions as the ALE. For each strain, we started with 0 PQ. OD measurements and samples were taken at various time points until stationary phase was reached. We then passaged the cells into a new flask, stepped up the PQ concentration, and characterized the next curve, for concentrations 125, 250, 500, 750, 1500, and 2500  $\mu\text{M}$ . We stopped if growth was not observed after 48 hours. For each flask, growth rates were determined by linear regression of  $\ln(\text{OD})$  versus time in the early exponential part of the curve.

We took cell culture samples at the same time as OD measurements for the starting strain at 0 and 125  $\mu\text{M}$  PQ, and for the evolved strains at 0, 250, and 750  $\mu\text{M}$  PQ. Samples were sterile filtered, and extracellular by-products were determined by high pressure liquid chromatography (HPLC). The filtrate was injected into an HPLC column (Aminex HPX-87H 125–0140). The concentrations of the detected compounds were determined by comparison to a normalized curve of known concentrations. Substrate uptake and secretion rates in the early exponential growth phase were calculated from the product of the growth rate and the slope from a linear regression of the grams (dry weight) (gDW) versus the substrate concentration. The biomass yield was calculated as the quotient of the growth rate and the glucose uptake rates during the exponential growth phase.

**RNA Sequencing**—3 mL of induced culture was added to 6 mL of RNAProtect Bacteria Reagent (Qiagen) and vortexed, then left at room temperature to incubate for 5 minutes. Cells were pelleted, resuspended in 400  $\mu\text{L}$  elution buffer, and then split into two tubes with one kept as a spare. One pellet was then lysed enzymatically with addition of lysozyme, proteinase-K, and 20% SDS. SUPERase-In was added to maintain the integrity of the RNA. RNA isolation was then performed according to the RNeasy Mini Kit (Qiagen) protocol. rRNA was depleted using the Ribo-Zero rRNA Removal Kit for gram negative bacteria according to the protocol. Libraries were constructed for paired-end sequencing using a KAPA RNAseq Library Preparation kit. Reads were sequenced on the Illumina NextSeq platform.



As part of the PRECISE-1K dataset<sup>47</sup>, transcriptomic reads were mapped using our pipeline (<https://github.com/avsastry/modulome-workflow>)<sup>32</sup> and run on Amazon Web Services Batch. First, raw read trimming was performed using Trim Galore with default options, followed by FastQC on the trimmed reads. Next, reads were aligned to the *E. coli* K-12 MG1655 reference genome (NC\_000913.3) using Bowtie<sup>80</sup>. The read direction was inferred using RSeQC<sup>81</sup>. Read counts were generated using featureCounts<sup>82</sup>. All quality control metrics were compiled using MultiQC<sup>83</sup>. Finally, the expression dataset was reported in units of log-transformed transcripts per million (log(TPM)).

All included samples passed rigorous quality control, with “high-quality” defined as (i) passing the following FastQC checks: *per\_base\_sequence\_quality*, *per\_sequence\_quality\_scores*, *per\_base\_n\_content*, *adaptor content*; (ii) having at least 500,000 reads mapped to the coding sequences of the reference genome (NC\_000913.3); (iii) not being an outlier in a hierarchical clustering based on pairwise Pearson correlation between all samples in PRECISE-1K; and (iv) having a minimum Pearson correlation between biological replicates of 0.95.

**Ribosome profiling**—Ribosome profiling libraries were created using a modified version of the protocol outlined in Latif *et al.*<sup>84</sup>. The protocol was modified to negate the effects of the addition of chloramphenicol by grinding frozen cells. 50 mL of cell culture was harvested by centrifugation for 4 minutes at 37°C in a 50 mL conical tube containing 0.4 g of sand. Supernatant was aspirated quickly and the pellet was flash frozen in liquid nitrogen. Pellets were transferred into a liquid nitrogen cooled mortar and pestle, 500 µL of lysis buffer was added, and the pellet was pulverized to lyse the cells. Lysate was transferred to a falcon tube to thaw on ice. The lysate was then centrifuged, and the supernatant was isolated to continue with the published protocol. Reads were sequenced on an Illumina HighSeq machine using a single end 50 bp kit.

Adaptors were removed from ribosome profiling reads using CutAdapt v1.8<sup>85</sup>, then mapped to the *E. coli* K-12 MG1655 reference genome (NC\_000913.3) using bowtie<sup>80</sup>. They were scored at the 3' end to generate ribosome density profiles.

**Generation of *pitA* mutant strains**—The mutations referred to in Figures 4H–K and S2 were introduced into the starting (0\_0) and evolved (1\_0) genomes using a Cas9-assisted Lambda Red homologous recombination method. Golden gate assembly was first used to construct a plasmid vector harboring both Cas9 and lambda red recombinase genes under the control of an L-arabinose inducible promoter, a single guide RNA sequence, and a donor fragment generated by PCR which contained the desired *pitA* +T mutation and around 200 bp flanking both sides of the Cas9 target cut site as directed by the guide RNA. After allowing cells harboring the plasmid to grow for 2 hours at 30°C, L-arabinose was added to the media and the cells were allowed to grow for 3 to 5 hours, at which time a portion of the culture was plated. Single colonies were screened using ARMS PCR. Amplicons spanning the mutation site, generated with primers annealing to the genome upstream and downstream of the sequence of the donor fragment contained in the plasmid, were confirmed with Sanger sequencing. Confirmed isolates were cured of the plasmid by growth at 37°C.

**Cell motility assay**—We performed motility assays in duplicate for each of the conditions shown in Figure S2. We mixed a tryptone broth (13 g tryptone and 7 g NaCl per liter of media) with 0.25% agar and the desired PQ level. We autoclaved the broths, then poured 25 mL into petri dishes and solidified them at room temperature overnight. Fresh colonies were spotted in the middle of the semi-solid agar with a toothpick. The plates were then incubated at 37°C for 6–8 hours and imaged on a Gel Imaging System.

### Quantification and statistical analysis

**iModulon computation and curation**—The full PRECISE-1K compendium, including the samples for this study, was used to compute iModulons using our previously described method<sup>47,86</sup>. The log(TPM) dataset  $\mathbf{X}$  was first centered such that wild-type *E. coli* MG1655 samples in M9 minimal media with glucose had expression values of 0 for all genes. Independent component analysis was performed using the Scikit-Learn (v0.19.0) implementation of FastICA<sup>87</sup>. We performed 100 iterations of the algorithm across a range of dimensionalities, and for each dimensionality we pooled and clustered the components with DBSCAN to find robust components which appeared in more than 50 of the iterations. If the dimensionality parameter is too high, ICA will begin to return single gene components; if it is too low, the components will be too dense to represent biological signals. Therefore, we selected a dimensionality which was as high as possible without creating many single gene components, as described<sup>86</sup>. At the optimal dimensionality, the total number of iModulons was 201. The output is composed of matrices  $\mathbf{M}$  [genes x iModulons], which defines the relationship between each iModulon and each gene, and  $\mathbf{A}$  [iModulons x samples], which contains the activity levels for each iModulon in each sample.

For each iModulon, a threshold must be drawn in the  $\mathbf{M}$  matrix to determine which genes are members of each iModulon. These thresholds are based on the distribution of gene weights. The highest weighted genes were progressively removed until the remaining weights had a D'agostino  $K^2$  normality below 550. Thus, the iModulon member genes are outliers from an otherwise normal distribution. iModulon annotation and curation was performed by comparing them against the known TRN from RegulonDB<sup>22</sup>. Names, descriptions, and statistics for each iModulon are available from the PRECISE-1K manuscript<sup>47</sup>, iModulonDB<sup>21</sup>, and Table S3.

**Differential iModulon activity analysis**—DiMAs were calculated as previously described<sup>20,32</sup>. For each iModulon, a null distribution was generated by calculating the absolute difference between each pair of biological replicates and fitting a log-normal distribution to them. For the groups being compared, their mean difference for each iModulon was compared to that iModulon's null distribution to obtain a p-value. The set of p-values for all iModulons was then false discovery rate (FDR) corrected to generate q-values. Activities were considered significant if they passed an absolute difference threshold of 5 and an FDR of 0.1. The main comparison in this study was between the starting strain at 250  $\mu\text{M}$  PQ ( $n = 2$ ) and the combined set of all evolved strains at 250 and 750  $\mu\text{M}$  PQ ( $n = 61$ ). Performing the comparison using both concentrations of PQ ensures that our comparison captures all of the major effects of tolerization. The set of DiMAs was similar when performing the comparison at just one or the other concentration.

We also performed a brief DEG analysis, which used the same algorithm as above but with individual gene expression values instead of iModulon activities. We used an FDR of 0.1 as above, and we scaled the fold change from its default value of 5 such that it was proportional to the range of values in the different matrices:  $\text{scaled\_thresh} = \text{default\_thresh} * (\text{Xmax} - \text{Xmin}) / (\text{Amax} - \text{Amin}) = 0.787$ .

**iModulon explained variance calculation**—The explained variance for each iModulon in this study was calculated using our workflow<sup>32</sup>. Since iModulons are built on a matrix decomposition, the contribution of each one to the overall expression dataset can be calculated. For each iModulon, the column of **M** and the row of **A** for the evolved samples in this study were multiplied together, and the explained variance between the result and the full expression dataset was computed. These explained variance scores were used to size the subsets of the treemap in Figure 1H. Note that the variance explained by ICA is ‘knowledge-based’ in contrast to the ‘statistic-based’ variance explanation provided by the commonly used principal component analysis (PCA).

**ME modeling**—We used OxidizeME, a genome-scale model of metabolism and expression (ME) with ROS damage responses<sup>3</sup>. Models used for flux maps were constrained using phenotypic data (glucose uptake rate and growth rate) and expression data as previously described<sup>11,12</sup>. In order to force PQ cycling in the model, the lower bounds for the ‘PQ2RED\_FWD\_FLAVONADPREDUCT-MONOMER\_mod\_fad’ and ‘PQ1OX\_FWD\_SPONT’ were set to the same non-zero value and iterated over. Additionally, the former reaction was amended to accept NADH as an electron donor by editing the stoichiometry. PQ cycling sweeping calculations were performed by sampling various lower bounds to identify the range the model could support growth, and then sweeping 100 uniform values within that range. The total NADH produced through the TCA cycle was calculated by summing the fluxes for the ‘MDH’ and ‘AKGDH’ metabolic reactions. The percentage of the proteome allocated to the TCA cycle was calculated using the solutions from each model, specifically the translation fluxes:

$$\% \text{ Proteome Allocated to the TCA cycle} = \frac{\sum_i mw_i * V_i^{\text{translation}}}{\sum_j mw_j * V_j^{\text{translation}}}$$

Where  $mw_i$  and  $V_i^{\text{translation}}$  represents the molecular weight and translation flux of the  $i$ th protein in the TCA cycle, and  $mw_j$  and  $V_j^{\text{translation}}$  represents the molecular weight and translation flux of the  $j$ th protein the entire model. The damaged portion of the proteome was calculated as follows:

$$\% \text{ Damaged Proteome Allocated to the TCA cycle} = \frac{\sum_k mw_k * V_k^{\text{complex formation}}}{\sum_j mw_j * V_j^{\text{translation}}}$$

Where  $mw_j$  and  $V_j^{\text{translation}}$  are the same variables above, and  $mw_k$  and  $V_k^{\text{complex formation}}$  correspond to the  $k$ th protein in Table S5. The undamaged portion of the proteome allocated to the TCA cycle was calculated as the difference between the total proteome allocated and the damaged proteome allocated.

## Supplementary Material

Refer to Web version on PubMed Central for supplementary material.

## Acknowledgements

This work was funded by the Novo Nordisk Foundation grant numbers NNF10CC1016517 and NNF20CC0035580, and by National Institute of General Medical Sciences grant number GM057089. It used resources of the National Energy Research Scientific Computing Center, a DOE Office of Science User Facility supported by the Office of Science of the U.S. Department of Energy under Contract No. DE-AC02-05CH11231. We would like to thank Marc Abrams for his assistance with manuscript editing and Lachlan Munro for assistance with wet lab experiments. We would also like to thank Daniel Zielinski, Lei Yang, Emre Ozdemir, Tobias Alter, Ke Chen, and Jayanth Krishnan for helpful discussions. We thank Jason Yang for invaluable discussions and advice on an early draft of this manuscript. The graphical abstract was created in Biorender.

## Inclusion and diversity

We support inclusive, diverse, and equitable conduct of research.

## References

1. Muir P, Li S, Lou S, Wang D, Spakowicz DJ, Salichos L, Zhang J, Weinstock GM, Isaacs F, Rozowsky J, et al. (2016). The real cost of sequencing: scaling computation to keep pace with data generation. *Genome Biol.* 17, 53. 10.1186/s13059-016-0917-0. [PubMed: 27009100]
2. Seif Y, and Palsson BØ (2021). Path to improving the life cycle and quality of genome-scale models of metabolism. *Cell Syst.* 12, 842–859. 10.1016/j.cels.2021.06.005. [PubMed: 34555324]
3. Yang L, Mih N, Anand A, Park JH, Tan J, Yurkovich JT, Monk JM, Lloyd CJ, Sandberg TE, Seo SW, et al. (2019). Cellular responses to reactive oxygen species are predicted from molecular mechanisms. *Proc. Natl. Acad. Sci. U. S. A* 116, 14368–14373. 10.1073/pnas.1905039116. [PubMed: 31270234]
4. Yang JH, Wright SN, Hamblin M, McCloskey D, Alcantar MA, Schrübbers L, Lopatkin AJ, Satish S, Nili A, Palsson BO, et al. (2019). A White-Box Machine Learning Approach for Revealing Antibiotic Mechanisms of Action. *Cell* 177, 1649–1661.e9. 10.1016/j.cell.2019.04.016. [PubMed: 31080069]
5. Subramanian I, Verma S, Kumar S, Jere A, and Anamika K (2020). Multi-omics Data Integration, Interpretation, and Its Application. *Bioinforma. Biol. Insights* 14, 1177932219899051. 10.1177/1177932219899051.
6. Sandberg TE, Salazar MJ, Weng LL, Palsson BO, and Feist AM (2019). The emergence of adaptive laboratory evolution as an efficient tool for biological discovery and industrial biotechnology. *Metab. Eng* 56, 1–16. 10.1016/j.ymben.2019.08.004. [PubMed: 31401242]
7. Peabody GL, Winkler J, and Kao KC (2014). Tools for developing tolerance to toxic chemicals in microbial systems and perspectives on moving the field forward and into the industrial setting. *Curr. Opin. Chem. Eng* 6, 9–17. 10.1016/j.coche.2014.08.001.
8. Phaneuf PV, Gosting D, Palsson BO, and Feist AM (2019). ALEdb 1.0: a database of mutations from adaptive laboratory evolution experimentation. *Nucleic Acids Res.* 47, D1164–D1171. 10.1093/nar/gky983. [PubMed: 30357390]
9. Hughes D, and Andersson DI (2015). Evolutionary consequences of drug resistance: shared principles across diverse targets and organisms. *Nat. Rev. Genet* 16, 459–471. 10.1038/nrg3922. [PubMed: 26149714]
10. Deatherage DE, and Barrick JE (2014). Identification of mutations in laboratory-evolved microbes from next-generation sequencing data using breseq. *Methods Mol. Biol.* Clifton NJ 1151, 165–188. 10.1007/978-1-4939-0554-6\_12.
11. Anand A, Olson CA, Sastry AV, Patel A, Szubin R, Yang L, Feist AM, and Palsson BO (2021). Restoration of fitness lost due to dysregulation of the pyruvate dehydrogenase complex is triggered

- by ribosomal binding site modifications. *Cell Rep.* 35, 108961. 10.1016/j.celrep.2021.108961. [PubMed: 33826886]
12. Anand A, Patel A, Chen K, Olson CA, Phaneuf PV, Lamoureux C, Hefner Y, Szubin R, Feist AM, and Palsson BO (2022). Laboratory evolution of synthetic electron transport system variants reveals a larger metabolic respiratory system and its plasticity. *Nat. Commun* 13, 3682. 10.1038/s41467-022-30877-5. [PubMed: 35760776]
  13. Monk JM, Lloyd CJ, Brunk E, Mih N, Sastry A, King Z, Takeuchi R, Nomura W, Zhang Z, Mori H, et al. (2017). iML1515, a knowledgebase that computes *Escherichia coli* traits. *Nat. Biotechnol* 35, 904–908. 10.1038/nbt.3956. [PubMed: 29020004]
  14. Chen K, Gao Y, Mih N, O'Brien EJ, Yang L, and Palsson BO (2017). Thermosensitivity of growth is determined by chaperone-mediated proteome reallocation. *Proc. Natl. Acad. Sci* 114, 11548–11553. 10.1073/pnas.1705524114. [PubMed: 29073085]
  15. Du B, Yang L, Lloyd CJ, Fang X, and Palsson BO (2019). Genome-scale model of metabolism and gene expression provides a multi-scale description of acid stress responses in *Escherichia coli*. *PLOS Comput. Biol* 15, e1007525. 10.1371/journal.pcbi.1007525. [PubMed: 31809503]
  16. Sandberg TE, Pedersen M, LaCroix RA, Ebrahim A, Bonde M, Herrgard MJ, Palsson BO, Sommer M, and Feist AM (2014). Evolution of *Escherichia coli* to 42 °C and subsequent genetic engineering reveals adaptive mechanisms and novel mutations. *Mol. Biol. Evol* 31, 2647–2662. 10.1093/molbev/msu209. [PubMed: 25015645]
  17. Phaneuf PV, Yurkovich JT, Heckmann D, Wu M, Sandberg TE, King ZA, Tan J, Palsson BO, and Feist AM (2020). Causal mutations from adaptive laboratory evolution are outlined by multiple scales of genome annotations and condition-specificity. *BMC Genomics* 21, 514. 10.1186/s12864-020-06920-4. [PubMed: 32711472]
  18. Myers KS, Park DM, Beauchene NA, and Kiley PJ (2015). Defining bacterial regulons using ChIP-seq. *Methods* 86, 80–88. 10.1016/j.ymeth.2015.05.022. [PubMed: 26032817]
  19. Browning DF, and Busby SJW (2016). Local and global regulation of transcription initiation in bacteria. *Nat. Rev. Microbiol* 14, 638–650. 10.1038/nrmicro.2016.103. [PubMed: 27498839]
  20. Sastry AV, Gao Y, Szubin R, Hefner Y, Xu S, Kim D, Choudhary KS, Yang L, King ZA, and Palsson BO (2019). The *Escherichia coli* transcriptome mostly consists of independently regulated modules. *Nat. Commun* 10. 10.1038/s41467-019-13483-w.
  21. Rychel K, Decker K, Sastry AV, Phaneuf PV, Poudel S, and Palsson BO (2020). iModulonDB: a knowledgebase of microbial transcriptional regulation derived from machine learning. *Nucleic Acids Res.* 10.1093/nar/gkaa810.
  22. Santos-Zavaleta A, Salgado H, Gama-Castro S, Sánchez-Pérez M, Gómez-Romero L, Ledezma-Tejeida D, García-Sotelo JS, Alquicira-Hernández K, Muñoz-Rascado LJ, Peña-Loredo P, et al. (2019). RegulonDB v 10.5: tackling challenges to unify classic and high throughput knowledge of gene regulation in *E. coli* K-12. *Nucleic Acids Res.* 47, D212–D220. 10.1093/nar/gky1077. [PubMed: 30395280]
  23. Lamoureux CR, Decker KT, Sastry AV, Rychel K, Gao Y, McConn JL, Zielinski DC, and Palsson BO (2021). A multi-scale transcriptional regulatory network knowledge base for *Escherichia coli* (Bioinformatics) 10.1101/2021.04.08.439047.
  24. Poudel S, Tsunemoto H, Seif Y, Sastry AV, Szubin R, Xu S, Machado H, Olson CA, Anand A, Pogliano J, et al. (2020). Revealing 29 sets of independently modulated genes in *Staphylococcus aureus*, their regulators, and role in key physiological response. *Proc. Natl. Acad. Sci* 117, 17228–17239. 10.1073/pnas.2008413117. [PubMed: 32616573]
  25. Rychel K, Sastry AV, and Palsson BO (2020). Machine learning uncovers independently regulated modules in the *Bacillus subtilis* transcriptome. *Nat. Commun* 11, 6338. 10.1038/s41467-020-20153-9. [PubMed: 33311500]
  26. Chauhan SM, Poudel S, Rychel K, Lamoureux C, Yoo R, Al Bulushi T, Yuan Y, Palsson BO, and Sastry AV (2021). Machine Learning Uncovers a Data-Driven Transcriptional Regulatory Network for the Crenarchaeal Thermoacidophile *Sulfolobus acidocaldarius*. *Front. Microbiol* 12.
  27. Lim HG, Rychel K, Sastry AV, Bentley GJ, Mueller J, Schindel HS, Larsen PE, Laible PD, Guss AM, Niu W, et al. (2022). Machine-learning from *Pseudomonas putida* KT2440 transcriptomes reveals its transcriptional regulatory network. *Metab. Eng* 10.1016/j.ymben.2022.04.004.

28. Rajput A, Tsunemoto H, Sastry AV, Szubin R, Rychel K, Sugie J, Pogliano J, and Palsson BO (2022). Machine learning from *Pseudomonas aeruginosa* transcriptomes identifies independently modulated sets of genes associated with known transcriptional regulators. *Nucleic Acids Res.* 50, 3658–3672. 10.1093/nar/gkac187. [PubMed: 35357493]
29. Yoo R, Rychel K, Poudel S, Al-Bulushi T, Yuan Y, Chauhan S, Lamoureux C, Palsson BO, and Sastry A (2022). Machine Learning of All *Mycobacterium tuberculosis* H37Rv RNA-seq Data Reveals a Structured Interplay between Metabolism, Stress Response, and Infection. *mSphere* 7, e0003322. 10.1128/msphere.00033-22. [PubMed: 35306876]
30. Rajput A, Tsunemoto H, Sastry AV, Szubin R, Rychel K, Chauhan SM, Pogliano J, and Palsson BO (2022). Advanced transcriptomic analysis reveals the role of efflux pumps and media composition in antibiotic responses of *Pseudomonas aeruginosa*. *Nucleic Acids Res.* 50, 9675–9688. 10.1093/nar/gkac743. [PubMed: 36095122]
31. Yuan Y, Seif Y, Rychel K, Yoo R, Chauhan S, Poudel S, Al-Bulushi T, Palsson BO, and Sastry AV (2022). Pan-Genome Analysis of Transcriptional Regulation in Six *Salmonella enterica* Serovar Typhimurium Strains Reveals Their Different Regulatory Structures. *mSystems*, e0046722. 10.1128/msystems.00467-22. [PubMed: 36317888]
32. Sastry AV, Poudel S, Rychel K, Yoo R, Lamoureux CR, Chauhan S, Haiman ZB, Bulushi TA, Seif Y, and Palsson BO (2021). Mining all publicly available expression data to compute dynamic microbial transcriptional regulatory networks. 2021.07.01.450581. 10.1101/2021.07.01.450581.
33. Anand A, Chen K, Yang L, Sastry AV, Olson CA, Poudel S, Seif Y, Hefner Y, Phaneuf PV, Xu S, et al. (2019). Adaptive evolution reveals a tradeoff between growth rate and oxidative stress during naphthoquinone-based aerobic respiration. *Proc. Natl. Acad. Sci* 116, 25287–25292. 10.1073/pnas.1909987116. [PubMed: 31767748]
34. Kavvas ES, Long CP, Sastry A, Poudel S, Antoniewicz MR, Ding Y, Mohamed ET, Szubin R, Monk JM, Feist AM, et al. (2022). Experimental Evolution Reveals Unifying Systems-Level Adaptations but Diversity in Driving Genotypes. *mSystems*, e0016522. 10.1128/msystems.00165-22. [PubMed: 36226969]
35. Anand A, Chen K, Catoi E, Sastry AV, Olson CA, Sandberg TE, Seif Y, Xu S, Szubin R, Yang L, et al. (2020). OxyR Is a Convergent Target for Mutations Acquired during Adaptation to Oxidative Stress-Prone Metabolic States. *Mol. Biol. Evol* 37, 660–667. 10.1093/molbev/msz251. [PubMed: 31651953]
36. Hassan HM, and Fridovich I (1979). Paraquat and *Escherichia coli*. Mechanism of production of extracellular superoxide radical. *J. Biol. Chem* 254, 10846–10852. 10.1016/S0021-9258(19)86598-5. [PubMed: 227855]
37. Imlay JA (2019). Where in the world do bacteria experience oxidative stress? *Environ. Microbiol* 21, 521–530. 10.1111/1462-2920.14445. [PubMed: 30307099]
38. Hassan HM, and Fridovich I (1979). Intracellular production of superoxide radical and of hydrogen peroxide by redox active compounds. *Arch. Biochem. Biophys* 196, 385–395. 10.1016/0003-9861(79)90289-3. [PubMed: 225995]
39. Fasnacht M, and Polacek N (2021). Oxidative Stress in Bacteria and the Central Dogma of Molecular Biology. *Front. Mol. Biosci* 8.
40. Imlay JA (2013). The molecular mechanisms and physiological consequences of oxidative stress: lessons from a model bacterium. *Nat. Rev. Microbiol* 11, 443–454. 10.1038/nrmicro3032. [PubMed: 23712352]
41. Imlay JA (2015). Diagnosing oxidative stress in bacteria: not as easy as you might think. *Curr. Opin. Microbiol* 24, 124–131. 10.1016/j.mib.2015.01.004. [PubMed: 25666086]
42. Schieber M, and Chandel NS (2014). ROS Function in Redox Signaling and Oxidative Stress. *Curr. Biol. CB* 24, R453–R462. 10.1016/j.cub.2014.03.034. [PubMed: 24845678]
43. LaCroix RA, Sandberg TE, O'Brien EJ, Utrilla J, Ebrahim A, Guzman GI, Szubin R, Palsson BO, and Feist AM (2015). Use of Adaptive Laboratory Evolution To Discover Key Mutations Enabling Rapid Growth of *Escherichia coli* K-12 MG1655 on Glucose Minimal Medium. *Appl. Environ. Microbiol* 81, 17–30. 10.1128/AEM.02246-14. [PubMed: 25304508]

44. LaCroix RA, Palsson BO, and Feist AM (2017). A Model for Designing Adaptive Laboratory Evolution Experiments. *Appl. Environ. Microbiol* 83, e03115–16. 10.1128/AEM.03115-16. [PubMed: 28159796]
45. Candeias LP, and Steenken S (1993). Electron transfer in di(deoxy)nucleoside phosphates in aqueous solution: rapid migration of oxidative damage (via adenine) to guanine. *J. Am. Chem. Soc* 115, 2437–2440. 10.1021/ja00059a044.
46. Foti JJ, Devadoss B, Winkler JA, Collins JJ, and Walker GC (2012). Oxidation of the guanine nucleotide pool underlies cell death by bactericidal antibiotics. *Science* 336, 315–319. 10.1126/science.1219192. [PubMed: 22517853]
47. Lamoureux CR, Decker KT, Sastry AV, McConn JL, Gao Y, and Palsson BO (2021). PRECISE 2.0 - an expanded high-quality RNA-seq compendium for *Escherichia coli* K-12 reveals high-resolution transcriptional regulatory structure 2021.04.08.439047. 10.1101/2021.04.08.439047.
48. Yerushalmi H, Lebendiker M, and Schuldiner S (1995). EmrE, an *Escherichia coli* 12-kDa multidrug transporter, exchanges toxic cations and H<sup>+</sup> and is soluble in organic solvents. *J. Biol. Chem* 270, 6856–6863. 10.1074/jbc.270.12.6856. [PubMed: 7896833]
49. Sekine Y, Aihara K, and Ohtsubo E (1999). Linearization and transposition of circular molecules of insertion sequence IS3. *J. Mol. Biol* 294, 21–34. 10.1006/jmbi.1999.3181. [PubMed: 10556026]
50. Mongkolsuk S, and Helmann JD (2002). Regulation of inducible peroxide stress responses. *Mol. Microbiol* 45, 9–15. 10.1046/j.1365-2958.2002.03015.x. [PubMed: 12100544]
51. Barshishat S, Elgrably-Weiss M, Edelstein J, Georg J, Govindarajan S, Haviv M, Wright PR, Hess WR, and Altuvia S (2018). OxyS small RNA induces cell cycle arrest to allow DNA damage repair. *EMBO J.* 37, 413–426. 10.15252/embj.201797651. [PubMed: 29237698]
52. Sastry AV, Dillon N, Anand A, Poudel S, Hefner Y, Xu S, Szubin R, Feist AM, Nizet V, and Palsson B (2021). Machine Learning of Bacterial Transcriptomes Reveals Responses Underlying Differential Antibiotic Susceptibility. *mSphere* 6, e00443–21. 10.1128/mSphere.00443-21. [PubMed: 34431696]
53. Smith AT, Linkous RO, Max NJ, Sestok AE, Szalai VA, and Chacón KN (2019). The FeoC [4Fe-4S] Cluster Is Redox-Active and Rapidly Oxygen-Sensitive. *Biochemistry* 58, 4935–4949. 10.1021/acs.biochem.9b00745. [PubMed: 31713418]
54. Rosenberg H, Gerdes RG, and Chegwidden K (1977). Two systems for the uptake of phosphate in *Escherichia coli*. *J. Bacteriol* 131, 505–511. 10.1128/jb.131.2.505-511.1977. [PubMed: 328484]
55. Prüss BM, Campbell JW, Van Dyk TK, Zhu C, Kogan Y, and Matsumura P (2003). FlhD/FlhC is a regulator of anaerobic respiration and the Entner-Doudoroff pathway through induction of the methyl-accepting chemotaxis protein Aer. *J. Bacteriol* 185, 534–543. 10.1128/JB.185.2.534-543.2003. [PubMed: 12511500]
56. Gottesman S (2019). Trouble is coming: Signaling pathways that regulate general stress responses in bacteria. *J. Biol. Chem* 294, 11685–11700. 10.1074/jbc.REV119.005593. [PubMed: 31197038]
57. Schellhorn HE (2020). Function, Evolution, and Composition of the RpoS Regulon in *Escherichia coli*. *Front. Microbiol* 11.
58. Kavvas ES, Antoniewicz M, Long C, Ding Y, Monk JM, Palsson BO, and Feist AM (2020). Laboratory evolution of multiple *E. coli* strains reveals unifying principles of adaptation but diversity in driving genotypes 2020.05.19.104992. 10.1101/2020.05.19.104992.
59. Utrilla J, O'Brien EJ, Chen K, McCloskey D, Cheung J, Wang H, Armenta-Medina D, Feist AM, and Palsson BO (2016). Global Rebalancing of Cellular Resources by Pleiotropic Point Mutations Illustrates a Multi-scale Mechanism of Adaptive Evolution. *Cell Syst.* 2, 260–271. 10.1016/j.cels.2016.04.003. [PubMed: 27135538]
60. Dalldorf C, Rychel K, Szubin R, Hefner Y, Patel A, Zielinski D, and Palsson B (2023). The hallmarks of a tradeoff in transcriptomes that balances stress and growth functions. *Res. Sq.* rs.3.rs-2729651. 10.21203/rs.3.rs-2729651/v1.
61. Zambrano MM, Siegele DA, Almirón M, Tormo A, and Kolter R (1993). Microbial Competition: *Escherichia coli* Mutants That Take Over Stationary Phase Cultures. *Science* 259, 1757–1760. 10.1126/science.7681219. [PubMed: 7681219]

62. Ferenci T, and Spira B (2007). Variation in stress responses within a bacterial species and the indirect costs of stress resistance. *Ann. N. Y. Acad. Sci* 1113, 105–113. 10.1196/annals.1391.003. [PubMed: 17483210]
63. Jang S, and Imlay JA (2007). Micromolar intracellular hydrogen peroxide disrupts metabolism by damaging iron-sulfur enzymes. *J. Biol. Chem* 282, 929–937. 10.1074/jbc.M607646200. [PubMed: 17102132]
64. Majumder A, Fang M, Tsai KJ, Ueguchi C, Mizuno T, and Wu HY (2001). LeuO expression in response to starvation for branched-chain amino acids. *J. Biol. Chem* 276, 19046–19051. 10.1074/jbc.M100945200. [PubMed: 11376008]
65. Jarrett JT (2005). The novel structure and chemistry of iron-sulfur clusters in the adenosylmethionine-dependent radical enzyme biotin synthase. *Arch. Biochem. Biophys* 433, 312–321. 10.1016/j.abb.2004.10.003. [PubMed: 15581586]
66. Beckett D (2007). Biotin sensing: universal influence of biotin status on transcription. *Annu. Rev. Genet* 41, 443–464. 10.1146/annurev.genet.41.042007.170450. [PubMed: 17669049]
67. Chen K, Anand A, Olson C, Sandberg TE, Gao Y, Mih N, and Palsson BO (2021). Bacterial fitness landscapes stratify based on proteome allocation associated with discrete aero-types. *PLOS Comput. Biol* 17, e1008596. 10.1371/journal.pcbi.1008596. [PubMed: 33465077]
68. Hill CW, Gray JA, and Brody H (1989). Use of the isocitrate dehydrogenase structural gene for attachment of e14 in *Escherichia coli* K-12. *J. Bacteriol* 171, 4083–4084. 10.1128/jb.171.7.4083-4084.1989. [PubMed: 2661545]
69. Fukushima T, Yamada K, Isobe A, Shiwaku K, and Yamane Y (1993). Mechanism of cytotoxicity of paraquat. I. NADH oxidation and paraquat radical formation via complex I. *Exp. Toxicol. Pathol. Off. J. Ges. Toxikol. Pathol* 45, 345–349. 10.1016/S0940-2993(11)80424-0.
70. Liochev SI, and Fridovich I (1994). Paraquat diaphorases in *Escherichia coli*. *Free Radic. Biol. Med* 16, 555–559. 10.1016/0891-5849(94)90055-8. [PubMed: 8026798]
71. Shimada H, Hirai K, Simamura E, and Pan J (1998). Mitochondrial NADH-quinone oxidoreductase of the outer membrane is responsible for paraquat cytotoxicity in rat livers. *Arch. Biochem. Biophys* 351, 75–81. 10.1006/abbi.1997.0557. [PubMed: 9500851]
72. Federowicz S, Kim D, Ebrahim A, Lerman J, Nagarajan H, Cho B, Zengler K, and Palsson B (2014). Determining the Control Circuitry of Redox Metabolism at the Genome-Scale. *PLOS Genet.* 10, e1004264. 10.1371/journal.pgen.1004264. [PubMed: 24699140]
73. Malpica R, Franco B, Rodriguez C, Kwon O, and Georgellis D (2004). Identification of a quinone-sensitive redox switch in the ArcB sensor kinase. *Proc. Natl. Acad. Sci* 101, 13318–13323. 10.1073/pnas.0403064101. [PubMed: 15326287]
74. Myers KS, Yan H, Ong IM, Chung D, Liang K, Tran F, Kele S, Landick R, and Kiley PJ (2013). Genome-scale Analysis of *Escherichia coli* FNR Reveals Complex Features of Transcription Factor Binding. *PLoS Genet.* 9, e1003565. 10.1371/journal.pgen.1003565. [PubMed: 23818864]
75. Saelens W, Cannoodt R, and Saeys Y (2018). A comprehensive evaluation of module detection methods for gene expression data. *Nat. Commun* 9. 10.1038/s41467-018-03424-4.
76. Rychel K (2022). SBRG/ROS-ALE: Pre-release for initial journal submission. 10.5281/ZENODO.7449004.
77. Mohamed ET, Wang S, Lennen RM, Herrgård MJ, Simmons BA, Singer SW, and Feist AM (2017). Generation of a platform strain for ionic liquid tolerance using adaptive laboratory evolution. *Microb. Cell Factories* 16, 204. 10.1186/s12934-017-0819-1.
78. Anand A, Olson CA, Yang L, Sastry AV, Catoiu E, Choudhary KS, Phaneuf PV, Sandberg TE, Xu S, Hefner Y, et al. (2019). Pseudogene repair driven by selection pressure applied in experimental evolution. *Nat. Microbiol* 4, 386–389. 10.1038/s41564-018-0340-2. [PubMed: 30692668]
79. Chen S, Huang T, Zhou Y, Han Y, Xu M, and Gu J (2017). AfterQC: automatic filtering, trimming, error removing and quality control for fastq data. *BMC Bioinformatics* 18, 80. 10.1186/s12859-017-1469-3. [PubMed: 28361673]
80. Langmead B, Trapnell C, Pop M, and Salzberg SL (2009). Ultrafast and memory-efficient alignment of short DNA sequences to the human genome. *Genome Biol.* 10, R25. 10.1186/gb-2009-10-3-r25. [PubMed: 19261174]



81. Wang L, Wang S, and Li W (2012). RSeQC: quality control of RNA-seq experiments. *Bioinforma. Oxf. Engl* 28, 2184–2185. 10.1093/bioinformatics/bts356.
82. Liao Y, Smyth GK, and Shi W (2014). featureCounts: an efficient general purpose program for assigning sequence reads to genomic features. *Bioinforma. Oxf. Engl* 30, 923–930. 10.1093/bioinformatics/btt656.
83. Ewels P, Magnusson M, Lundin S, and Källér M (2016). MultiQC: summarize analysis results for multiple tools and samples in a single report. *Bioinforma. Oxf. Engl* 32, 3047–3048. 10.1093/bioinformatics/btw354.
84. Latif H, Szubin R, Tan J, Brunk E, Lechner A, Zengler K, and Palsson BO (2015). A streamlined ribosome profiling protocol for the characterization of microorganisms. *BioTechniques* 58, 329–332. 10.2144/000114302. [PubMed: 26054770]
85. Martin M (2011). Cutadapt removes adapter sequences from high-throughput sequencing reads. *EMBnet.journal* 17, 10–12. 10.14806/ej.17.1.200.
86. McConn JL, Lamoureux CR, Poudel S, Palsson BO, and Sastry AV (2021). Optimal dimensionality selection for independent component analysis of transcriptomic data. *BMC Bioinformatics* 22, 584. 10.1186/s12859-021-04497-7. [PubMed: 34879815]
87. Pedregosa F Scikit-learn: Machine Learning in Python. *Mach. Learn PYTHON*, 6.
88. Grindley ND (1978). IS1 insertion generates duplication of a nine base pair sequence at its target site. *Cell* 13, 419–426. 10.1016/0092-8674(78)90316-1. [PubMed: 350412]
89. Klepsch MM, Kovermann M, Löw C, Balbach J, Permentier HP, Fusetti F, de Gier JW, Slotboom DJ, and Berntsson RP-A (2011). Escherichia coli peptide binding protein OppA has a preference for positively charged peptides. *J. Mol. Biol* 414, 75–85. 10.1016/j.jmb.2011.09.043. [PubMed: 21983341]
90. Freddolino PL, Amini S, and Tavazoie S (2012). Newly identified genetic variations in common Escherichia coli MG1655 stock cultures. *J. Bacteriol* 194, 303–306. 10.1128/JB.06087-11. [PubMed: 22081388]
91. Schnetz K, and Rak B (1992). IS5: a mobile enhancer of transcription in Escherichia coli. *Proc. Natl. Acad. Sci. U. S. A* 89, 1244–1248. 10.1073/pnas.89.4.1244. [PubMed: 1311089]
92. Sen A, and Imlay JA (2021). How Microbes Defend Themselves From Incoming Hydrogen Peroxide. *Front. Immunol* 12.
93. Bagg A, and Neilands JB (1987). Ferric uptake regulation protein acts as a repressor, employing iron (II) as a cofactor to bind the operator of an iron transport operon in Escherichia coli. *Biochemistry* 26, 5471–5477. 10.1021/bi00391a039. [PubMed: 2823881]
94. Esquilin-Lebron K, Dubrac S, Barras F, and Boyd JM (2021). Bacterial Approaches for Assembling Iron-Sulfur Proteins. *mBio* 12, e02425–21. 10.1128/mBio.02425-21. [PubMed: 34781750]
95. Blanc B, Clémancey M, Latour J-M, Fontecave M, and Ollagnier de Choudens S (2014). Molecular Investigation of Iron–Sulfur Cluster Assembly Scaffolds under Stress. *Biochemistry* 53, 7867–7869. 10.1021/bi5012496. [PubMed: 25485887]
96. Blanc B, Gerez C, and Ollagnier de Choudens S (2015). Assembly of Fe/S proteins in bacterial systems: Biochemistry of the bacterial ISC system. *Biochim. Biophys. Acta* 1853, 1436–1447. 10.1016/j.bbamcr.2014.12.009. [PubMed: 25510311]
97. Garcia PS, Gribaldo S, Py B, and Barras F (2019). The SUF system: an ABC ATPase-dependent protein complex with a role in Fe-S cluster biogenesis. *Res. Microbiol* 170, 426–434. 10.1016/j.resmic.2019.08.001. [PubMed: 31419582]
98. Roche B, Aussel L, Ezraty B, Mandin P, Py B, and Barras F (2013). Iron/sulfur proteins biogenesis in prokaryotes: Formation, regulation and diversity. *Biochim. Biophys. Acta BBA - Bioenerg* 1827, 455–469. 10.1016/j.bbabi.2012.12.010.
99. Rajagopalan S, Teter SJ, Zwart PH, Brennan RG, Phillips KJ, and Kiley PJ (2013). Studies of IscR reveal a unique mechanism for metal-dependent regulation of DNA binding specificity. *Nat. Struct. Mol. Biol* 20, 740. 10.1038/nsmb.2568. [PubMed: 23644595]
100. Lénon M, Arias-Cartín R, and Barras F (2022). The Fe–S proteome of Escherichia coli: prediction, function, and fate. *Metallomics* 14, mfac022. 10.1093/mtomcs/mfac022.

101. Touati D (2000). Sensing and protecting against superoxide stress in *Escherichia coli*--how many ways are there to trigger soxRS response? *Redox Rep. Commun. Free Radic. Res* 5, 287–293. 10.1179/135100000101535825.
102. Bibikov SI, Biran R, Rudd KE, and Parkinson JS (1997). A signal transducer for aerotaxis in *Escherichia coli*. *J. Bacteriol* 179, 4075–4079. 10.1128/jb.179.12.4075-4079.1997. [PubMed: 9190831]
103. Taylor BL, Zhulin IB, and Johnson MS (1999). Aerotaxis and other energy-sensing behavior in bacteria. *Annu. Rev. Microbiol* 53, 103–128. 10.1146/annurev.micro.53.1.103. [PubMed: 10547687]
104. Pesavento C, and Hengge R (2012). The global repressor FlhZ antagonizes gene expression by  $\sigma$ S-containing RNA polymerase due to overlapping DNA binding specificity. *Nucleic Acids Res.* 40, 4783–4793. 10.1093/nar/gks055. [PubMed: 22323519]
105. Irving SE, Choudhury NR, and Corrigan RM (2020). The stringent response and physiological roles of (pp)pGpp in bacteria. *Nat. Rev. Microbiol*, 1–16. 10.1038/s41579-020-00470-y. [PubMed: 31740776]
106. Mauzy CA, and Hermodson MA (1992). Structural and functional analyses of the repressor, RbsR, of the ribose operon of *Escherichia coli*. *Protein Sci. Publ. Protein Soc* 1, 831–842. 10.1002/pro.5560010701.
107. Christodoulou D, Link H, Fuhrer T, Kochanowski K, Gerosa L, and Sauer U (2018). Reserve Flux Capacity in the Pentose Phosphate Pathway Enables *Escherichia coli*'s Rapid Response to Oxidative Stress. *Cell Syst.* 6, 569–578.e7. 10.1016/j.cels.2018.04.009. [PubMed: 29753645]
108. Choi KY, and Zalkin H (1992). Structural characterization and corepressor binding of the *Escherichia coli* purine repressor. *J. Bacteriol* 174, 6207–6214. [PubMed: 1400170]
109. Lochowska A, Iwanicka-Nowicka R, Plochocka D, and Hryniewicz MM (2001). Functional dissection of the LysR-type CysB transcriptional regulator. Regions important for DNA binding, inducer response, oligomerization, and positive control. *J. Biol. Chem* 276, 2098–2107. 10.1074/jbc.M007192200. [PubMed: 11038360]
110. Ostrowski J, and Kredich NM (1990). In vitro interactions of CysB protein with the cysJIIH promoter of *Salmonella typhimurium*: inhibitory effects of sulfide. *J. Bacteriol* 172, 779–785. 10.1128/jb.172.2.779-785.1990. [PubMed: 2105304]
111. Leichert LI, Gehrke F, Gudiseva HV, Blackwell T, Ilbert M, Walker AK, Strahler JR, Andrews PC, and Jakob U (2008). Quantifying changes in the thiol redox proteome upon oxidative stress in vivo. *Proc. Natl. Acad. Sci* 105, 8197–8202. 10.1073/pnas.0707723105. [PubMed: 18287020]
112. Ohtsu I, Wiriyathanawudhiwong N, Morigasaki S, Nakatani T, Kadokura H, and Takagi H (2010). The l-Cysteine/l-Cystine Shuttle System Provides Reducing Equivalents to the Periplasm in *Escherichia coli*. *J. Biol. Chem* 285, 17479–17487. 10.1074/jbc.M109.081356. [PubMed: 20351115]
113. Rensing C, and Grass G (2003). *Escherichia coli* mechanisms of copper homeostasis in a changing environment. *FEMS Microbiol. Rev* 27, 197–213. 10.1016/S0168-6445(03)00049-4. [PubMed: 12829268]
114. Benov L, Sage H, and Fridovich I (1997). The copper- and zinc-containing superoxide dismutase from *Escherichia coli*: molecular weight and stability. *Arch. Biochem. Biophys* 340, 305–310. 10.1006/abbi.1997.9940. [PubMed: 9143335]
115. Cunin R, Eckhardt T, Piette J, Boyen A, Piérard A, and Glansdorff N (1983). Molecular basis for modulated regulation of gene expression in the arginine regulon of *Escherichia coli* K-12. *Nucleic Acids Res.* 11, 5007–5019. 10.1093/nar/11.15.5007. [PubMed: 6348703]
116. Chattopadhyay MK, Tabor CW, and Tabor H (2009). Polyamines are not required for aerobic growth of *Escherichia coli*: preparation of a strain with deletions in all of the genes for polyamine biosynthesis. *J. Bacteriol* 191, 5549–5552. 10.1128/JB.00381-09. [PubMed: 19542271]
117. Wu WH, and Morris DR (1973). Biosynthetic arginine decarboxylase from *Escherichia coli*. Subunit interactions and the role of magnesium ion. *J. Biol. Chem* 248, 1696–1699. [PubMed: 4571774]

118. Korkmaz G, Holm M, Wiens T, and Sanyal S (2014). Comprehensive Analysis of Stop Codon Usage in Bacteria and Its Correlation with Release Factor Abundance. *J. Biol. Chem* 289, 30334–30342. 10.1074/jbc.M114.606632. [PubMed: 25217634]
119. Rould MA, Perona JJ, Söll D, and Steitz TA (1989). Structure of *E. coli* Glutamyl-tRNA Synthetase Complexed with tRNAGln and ATP at 2.8 Å Resolution. *Science* 246, 1135–1142. 10.1126/science.2479982. [PubMed: 2479982]
120. Eggertsson G, and Söll D (1988). Transfer ribonucleic acid-mediated suppression of termination codons in *Escherichia coli*. *Microbiol. Rev* 52, 354–374. [PubMed: 3054467]
121. Liochev SI, Hausladen A, Beyer WF, and Fridovich I (1994). NADPH: ferredoxin oxidoreductase acts as a paraquat diaphorase and is a member of the soxRS regulon. *Proc. Natl. Acad. Sci* 91, 1328–1331. 10.1073/pnas.91.4.1328. [PubMed: 8108411]
122. Sauer U, Canonaco F, Heri S, Perrenoud A, and Fischer E (2004). The soluble and membrane-bound transhydrogenases UdhA and PntAB have divergent functions in NADPH metabolism of *Escherichia coli*. *J. Biol. Chem* 279, 6613–6619. 10.1074/jbc.M311657200. [PubMed: 14660605]
123. Kiley PJ, and Beinert H (1998). Oxygen sensing by the global regulator, FNR: the role of the iron-sulfur cluster. *FEMS Microbiol. Rev* 22, 341–352. 10.1111/j.1574-6976.1998.tb00375.x. [PubMed: 9990723]
124. Ramseier TM (1996). Cra and the control of carbon flux via metabolic pathways. *Res. Microbiol* 147, 489–493. 10.1016/0923-2508(96)84003-4. [PubMed: 9084760]
125. Kim D, Seo SW, Gao Y, Nam H, Guzman GI, Cho B-K, and Palsson BO (2018). Systems assessment of transcriptional regulation on central carbon metabolism by Cra and CRP. *Nucleic Acids Res.* 46, 2901–2917. 10.1093/nar/gky069. [PubMed: 29394395]
126. Kochanowski K, Volkmer B, Gerosa L, Haverkorn van Rijsewijk BR, Schmidt A, and Heinemann M (2013). Functioning of a metabolic flux sensor in *Escherichia coli*. *Proc. Natl. Acad. Sci. U. S. A* 110, 1130–1135. 10.1073/pnas.1202582110. [PubMed: 23277571]
127. Zheng D, Constantinidou C, Hobman JL, and Minchin SD (2004). Identification of the CRP regulon using in vitro and in vivo transcriptional profiling. *Nucleic Acids Res.* 32, 5874–5893. 10.1093/nar/gkh908. [PubMed: 15520470]
128. Green J, Stapleton MR, Smith LJ, Artymiuk PJ, Kahramanoglou C, Hunt DM, and Buxton RS (2014). Cyclic-AMP and bacterial cyclic-AMP receptor proteins revisited: adaptation for different ecological niches. *Curr. Opin. Microbiol* 18, 1–7. 10.1016/j.mib.2014.01.003. [PubMed: 24509484]
129. Miyake Y, Inaba T, Watanabe H, Teramoto J, Yamamoto K, and Ishihama A (2019). Regulatory roles of pyruvate-sensing two-component system PyrSR (YpdAB) in *Escherichia coli* K-12. *FEMS Microbiol. Lett* 366. 10.1093/femsle/fnz009.

## Additional resources

iModulonDB: [http://imodulondb.org/dataset.html?organism=e\\_coli&dataset=precise1k](http://imodulondb.org/dataset.html?organism=e_coli&dataset=precise1k)

ALEdb: [http://aledb.org/stats/?ale\\_experiment\\_id=1540](http://aledb.org/stats/?ale_experiment_id=1540)

### Highlights

- Adaptive laboratory evolution of *E. coli* generated strains which tolerate paraquat
- Mutation analysis revealed a high level of parallel evolution across the replicates
- iModulon analysis of transcriptomes provided detailed novel insights into evolution
- Six paraquat and ROS stress tolerance mechanisms from the strains were revealed

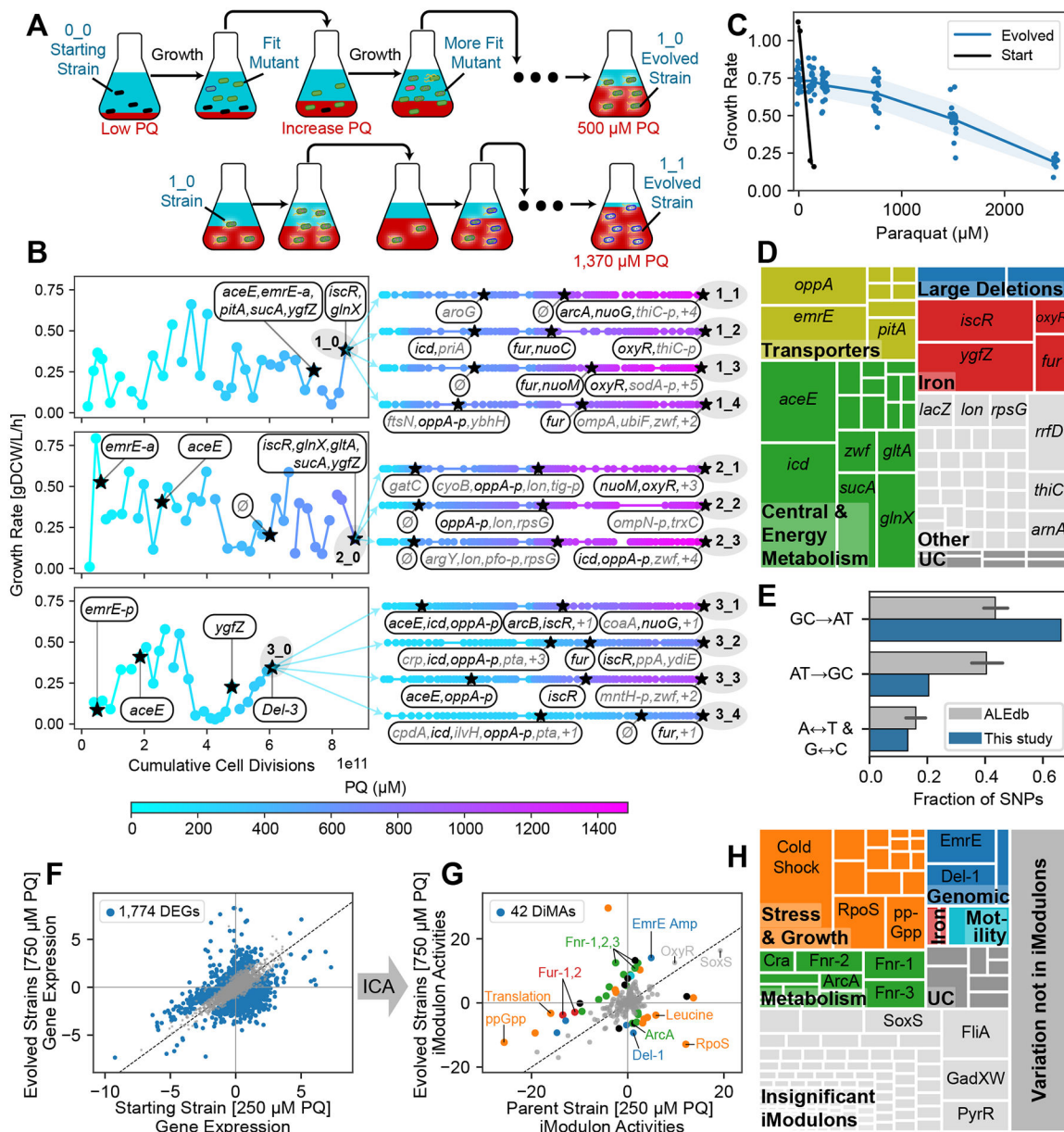


**Figure 1. ALE increases PQ tolerance via changes to the genome and transcriptome.**

(A) Tolerization ALE process, showing mutant strains (cells with various appearances) in media with increasing stress concentrations (red). Example replicates are shown: 1\_0 in the first generation and 1\_1 in the second generation. (B) Points represent ALE flasks colored by PQ concentration. The first generation of ALEs (strains 1\_0, 2\_0, and 3\_0) are shown with each flask's growth rate in grams dry cell weight per liter per hour (gDCW/L/h). 'Cumulative cell divisions' are estimated from the growth rate and time elapsed. Stars represent flasks that underwent DNA sequencing, and newly mutated genes are shown. Black colored genes are discussed in detail. (C) Growth rate for each strain at each PQ concentration. The starting strain cannot grow at 250 μM PQ, whereas some evolved strains reach up to 2500 μM PQ. Evolved strains grow slower than the starting strain in the absence

of PQ. **(D)** Treemap of mutations in all strains, grouped by gene with intergenic mutations assigned to nearest genes. UC: Uncharacterized. See Table S2, Methods. **(E)** Fraction of SNP types in this study compared with all public ALE studies on ALEdb ([aledb.org](http://aledb.org); mean  $\pm$  95% confidence interval, n = 54). Each label corresponds to four of the twelve possible substitutions; for instance, “GC $\rightarrow$ AT” includes “G $\rightarrow$ A”, “G $\rightarrow$ T”, “C $\rightarrow$ A” and “C $\rightarrow$ T” substitutions. This study is enriched for mutations which decrease the GC content of the genome. **(F-G)** Comparison between the mean transcriptomes of the parent strain at 250  $\mu$ M PQ vs. all evolved strains at 250 and 750  $\mu$ M PQ. **(F)** DEG analysis with FDR = 0.1 and a minimum fold change of 0.78 (Methods), showing an intractably large number of DEGs. **(G)** Differential iModulon activity (DiMA) analysis, which compresses the differential transcriptomic changes into 42 DiMAs. DiMAs are colored by their category from panel (H). For more information about each iModulon, explore the PRECISE-1K E. coli dataset at [iModulonDB.org](http://iModulonDB.org) and see Table S2. **(H)** Treemap of the explained variance of each iModulon in the transcriptome of the evolved strains (see Methods). The map is first broken into three parts: the colorful region, composed of iModulons that are differentially activated after the evolution and categorized, the light gray region composed of iModulons that do not show a significant trend with evolution, and the dark gray region, representing the error in the iModulon decomposition.

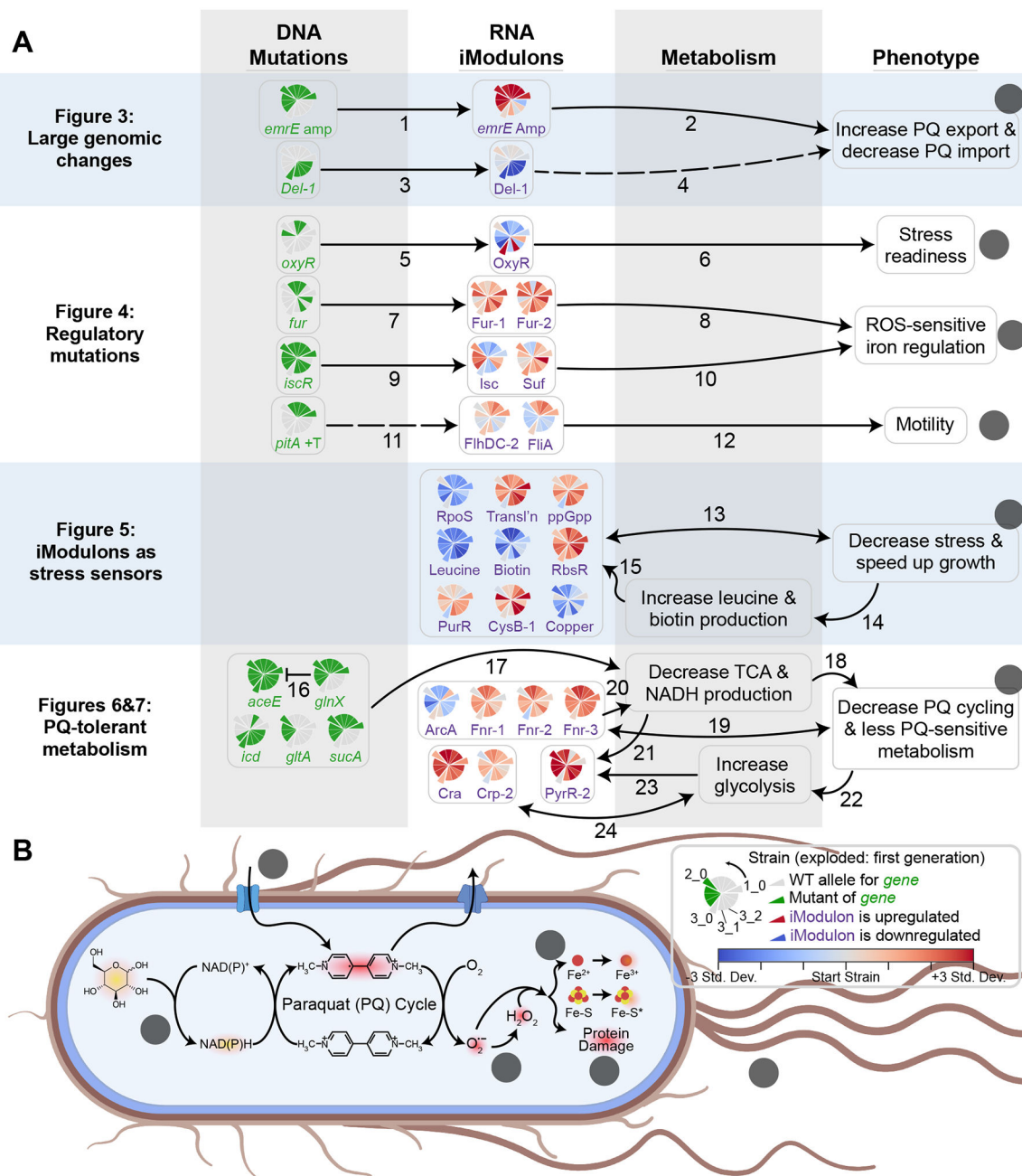


**Figure 2. Multilevel approach reveals mechanisms of PQ tolerance.**

(A) Knowledge graph summarizing multilevel relationships between mutations, iModulons, metabolism, and phenotypes. Pie charts appearing in the two left columns indicate prevalence of given changes to the genome and transcriptome (legend in panel B), where wedges indicate strains. The protruding wedges correspond to the first generation of ALEs, with the wedges counterclockwise to them being their second generation descendants. For genes, green indicates the strain has mutations affecting it or its promoter. For iModulons, colors indicate the difference between the iModulon activity in the strain at 750  $\mu\text{M}$  PQ and the starting strain at 250  $\mu\text{M}$  PQ, normalized to the standard deviation of the iModulon

activity across all of PRECISE-1K. Solid arrows represent hypothetical relationships with extensive experimental evidence, whereas dashed lines represent relationships for which there is little existing literature. Each arrow is labeled with a numeral corresponding to a row in Table S4 that describes the meaning, data evidence, literature evidence, and novelty of the corresponding relationship. **(B)** Phenotypic changes target specific processes involved in PQ and ROS stress. Lowercase letters indicate elements from the rightmost column of (A). Entities which glow are reduced, and red indicates stress-related molecules.



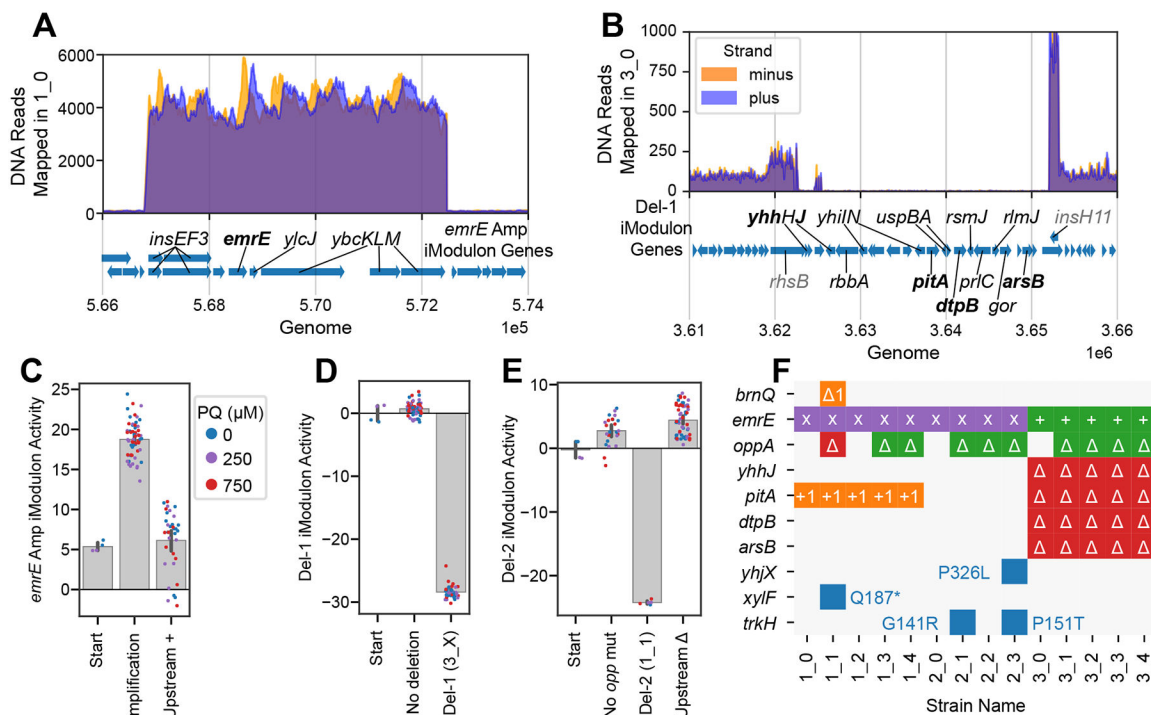


**Figure 3. Consequences of deletions and amplifications affecting membrane transport are found in both genomes and transcriptomes.**

(A) Number of reads mapped to the region around *emrE* in strain 1\_0, which is representative of strains containing the *emrE* amplification. Genes in the iModulon are labeled. (B) Number of reads from strain 3\_0 mapped in the region of Del-1. Del-1 iModulon genes are shown in black, with flanking non-deleted, non-iModulon genes in gray, and transporters in bold. (C-E) iModulon activities for selected genomic iModulons. Bars indicate mean ± 95% confidence interval. Individual samples are color-coded by PQ concentration. Upstream + and Δ indicate insertions and deletions, respectively. (F) Color-coded table showing all observed mutations related to transporter genes. Purple x: amplification; green: upstream insertion (+) or deletion (Δ); blue: indicated SNP; orange: frameshift mutation within gene; red delta: complete gene deletion (See Table S2 for more details on each mutation).

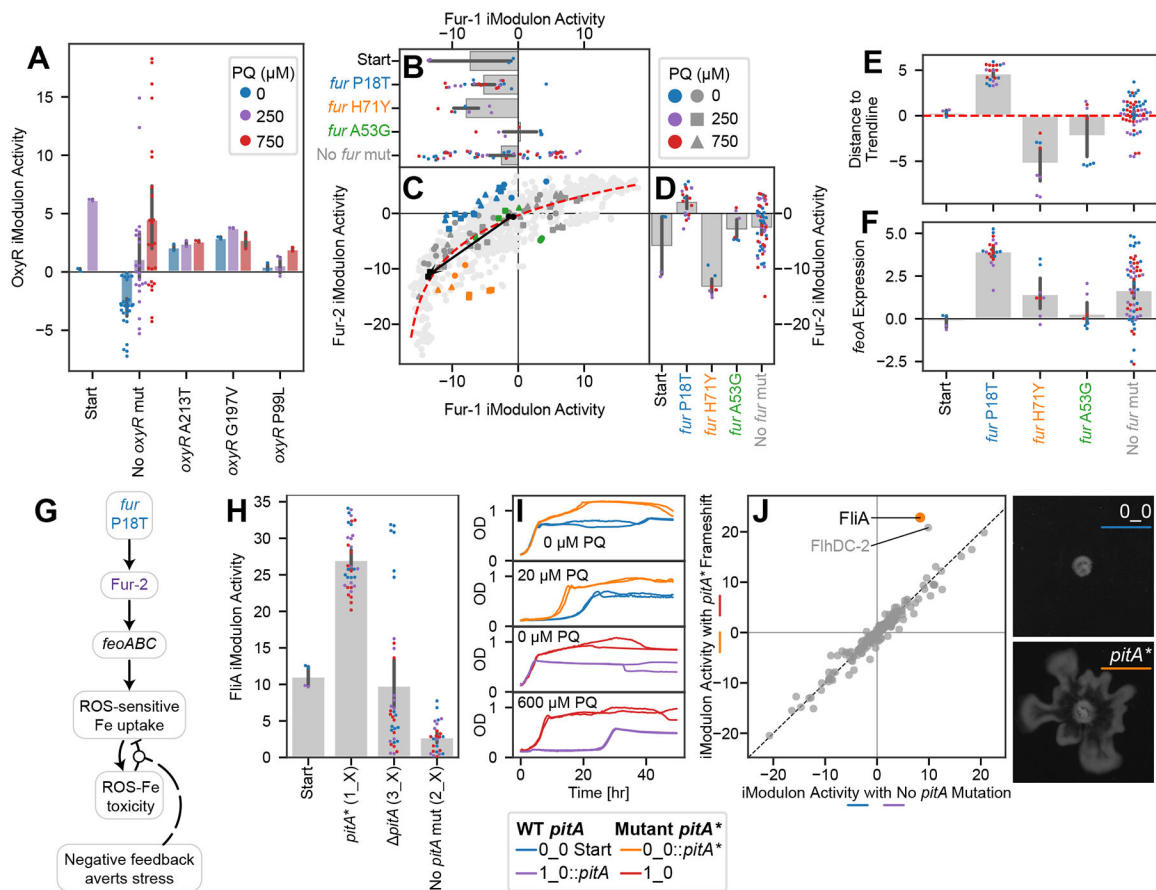


**Figure 4. Mutations regulate stress response, iron metabolism, and motility iModulons in novel ways.**

Bars indicate mean  $\pm$  95% confidence interval. **(A)** OxyR iModulon activity is correlated with PQ in starting and evolved strains (Pearson  $R = 0.47$ ,  $p = 6.2 \times 10^{-5}$ ), except for the three strains which mutated oxyR. PQ colors in the legend also apply to panels (B, D, E-F, H). **(B-D)** Scatter plot of Fur-1 and Fur-2 iModulon activities with bar plots sharing axes. Light gray dots indicate other samples from PRECISE-1K. In (C), samples are colored by relevant mutations, and shapes indicate PQ concentrations according to the legends. A black arrow connects the starting strain samples between 0 and 250  $\mu\text{M}$  PQ. In bar plots, point colors indicate PQ concentrations and label colors match with the scatter plots. The red trend line is a logarithmic curve fit to all samples in PRECISE-1K. Samples with the P18T mutation are above the trend line, indicating a preference for Fur-2. **(E)** Distances from each sample in this study to the trend line in (B), more clearly showing the preference for Fur-2 induced by P18T. **(F)** *feoA* expression, which is representative of the *feoABC* operon. Genes are upregulated by the fur P18T mutation. **(G)** Knowledge graph linking fur mutation to negative feedback which averts stress. **(H)** FliA iModulon activities by *pitA* mutation, showing an upregulation in the case of the frameshift *pitA\**, but not in the case of *pitA* deletion. **(I)** Growth curves for strains with and without the *pitA\** mutation as the only difference. The mutation contributes to higher final ODs under no stress, and shorter lag and faster growth under stress. **(J)** DiMA for strains 0\_0 and 1\_0 with and without the *pitA* frameshift mutation under PQ stress. Points indicate the mean of all relevant samples

(individual conditions in duplicate; n=6 per axis). The strains with the mutation significantly activate FliA, one of the motility iModulons. The point near FliA is FlhDC-2, the other major motility iModulon. **(K)** Representative images of swarming in the 0\_0 strain with (bottom) and without (top) the *pitA*\* frameshift. Scale bars: 1 cm. Additional plots: Figure S1; Images for all swarming experiments: Figure S2.

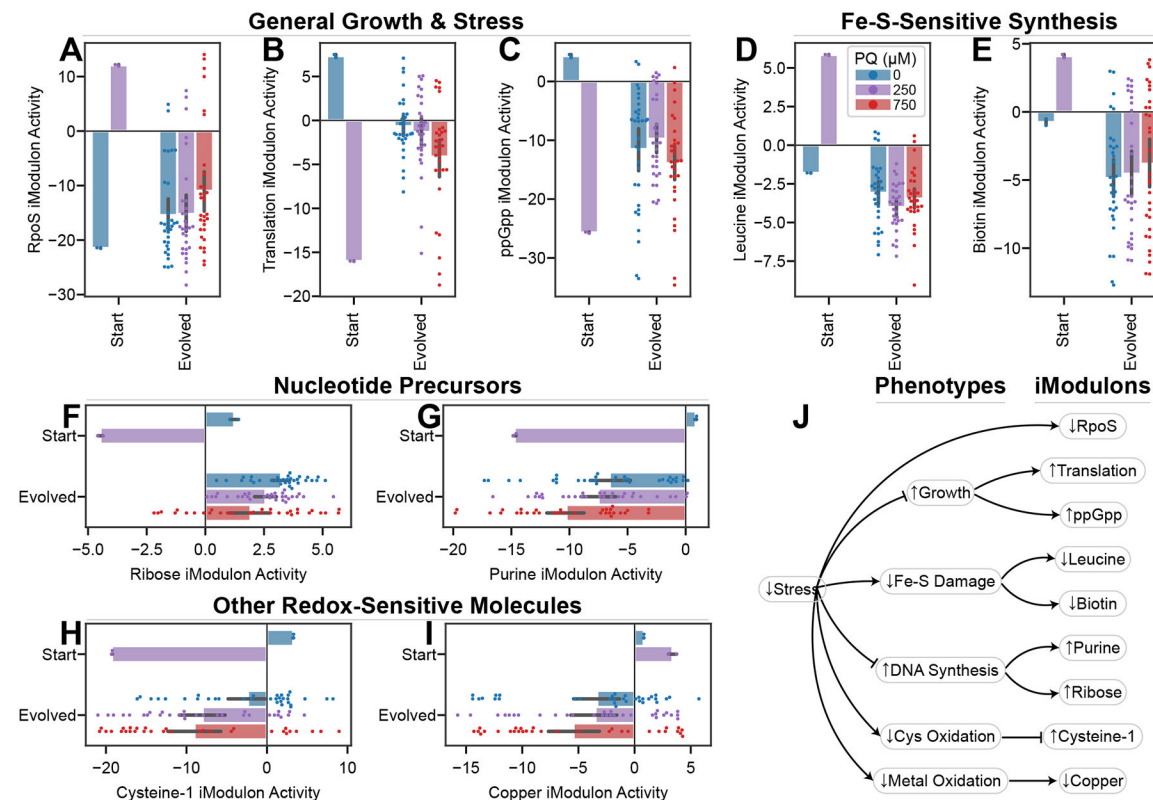


**Figure 5. Changes to stress and growth explain the changes to activity in several iModulons.** Mean iModulon activities  $\pm$  95% confidence interval; all plots use the legend in (D). P-values are false discovery rate corrected p-values from a DiMA comparison of stressed transcriptomes (250 and/or 750  $\mu$ M PQ) between 0\_0 and evolved strains. **(A)** RpoS activity, the general stress response, is downregulated ( $p = 0.017$ ). **(B)** The Translation iModulon, ribosomes and translation machinery, is upregulated ( $p = 0.023$ ). **(C)** The ppGpp iModulon, with many growth-related functions, follows a similar pattern to the Translation iModulon ( $p = 0.027$ ). **(D)** The Leucine iModulon, which responds to leucine concentrations downstream of an Fe-S-dependent synthesis pathway, is downregulated after evolution, suggesting improved Fe-S metabolism ( $p = 0.0017$ ). **(E)** The Biotin iModulon is downregulated after evolution. Biotin also depends on Fe-S-dependent synthesis ( $q = 0.017$ ). **(F-I)** Ribose ( $p = 0.011$ ), Purine ( $p = 0.036$ ), Cysteine-1 ( $p = 0.025$ ), and Copper ( $p = 0.034$ ) iModulon activities behave differently in starting and evolved strains (Supplementary Data S1 – Note S5). **(L)** Knowledge graph connecting decreased oxidative stress to each of the iModulon changes shown.

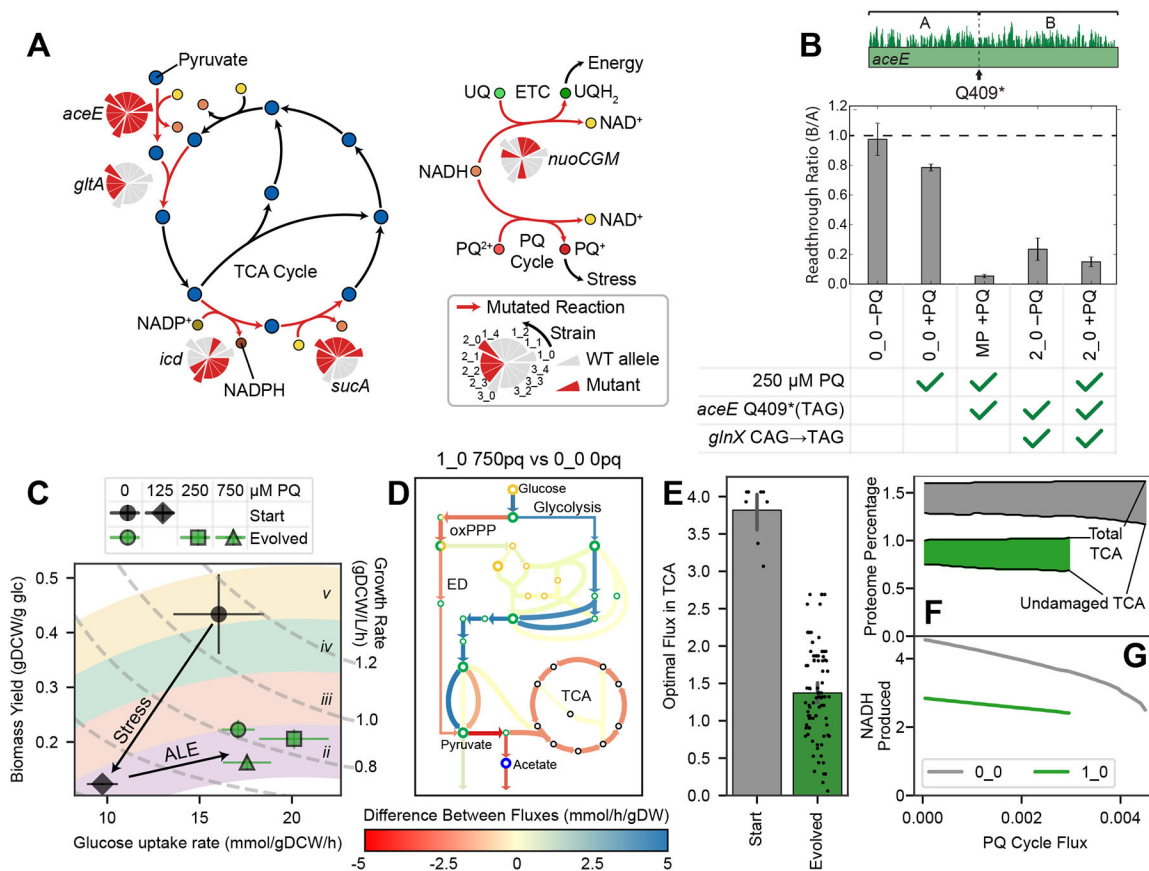


**Figure 6. Mutations drive metabolic rerouting toward fermentation to avoid PQ cycling by decreasing NADH availability.**

(A) Simplified metabolic map of the TCA cycle and fate of NADH. Reactions catalyzed by mutated enzymes are shown in red and labeled with a pie chart indicating which strains have a wild-type (WT) or mutant allele. First generation strains in the pie chart protrude, with their descendants following them counter-clockwise. (B) Ribosome readthrough ratio in *aceE* from ribosome profiling, means ± standard deviation, n = 3. The ratio B/A is the fraction of ribosomes bound downstream (B) vs. upstream (A) of the early amber stop codon (TAG) in *aceE*. The midpoint (MP) strain has *aceE* Q409\* with WT *glnX*, whereas the 2\_0 strain has both *aceE* Q409\* and the *glnX* anticodon mutation that enables ribosomes to read through the amber stop codon. In evolved strains such as 2\_0, PDH levels are decreased but not zero. (C) Aero-type plot<sup>67</sup> computed from measured growth rates and glucose uptake rates, where points represent means ± SEM (strains in duplicate; black n = 2, green n = 26), with constant growth rate isoclines. Colored regions labeled with roman numerals are aero-type regions as defined previously<sup>12</sup>. Cells switch to a lower aero-type with PQ and increase their glucose uptake after evolution. (D) Flux differences from the OxidizeME model, comparing the starting strain with no PQ and a representative evolved strain at high PQ. Model was constrained by growth rate, glucose uptake rate, and RNAseq data (Figure S4). (E) Each point represents a TCA cycle reaction in the constrained OxidizeME models; models of evolved strains predict lower TCA cycle fluxes. (F-G) OxidizeME model results in mmol/gDCW/h for 0\_0 and 1\_0, constrained by growth rate, glucose uptake rate, and

RNA expression. (F) As PQ cycle flux increases, the damaged fraction (filled in) of the TCA cycle increases. (G) NADH production decreases with PQ, but is more sensitive in 0\_0. 0\_0 can also carry more PQ cycle flux.

Author Manuscript

Author Manuscript

Author Manuscript

Author Manuscript

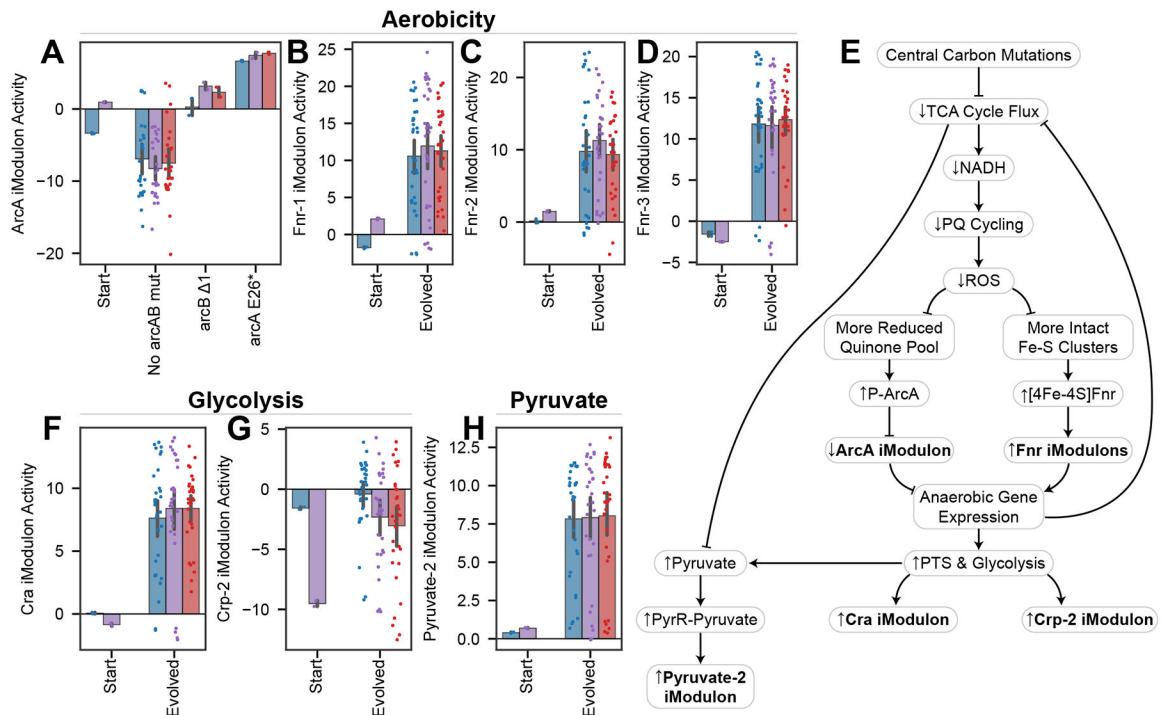


**Figure 7. Mutations and iModulon reallocation drive metabolic rerouting toward fermentation to avoid PQ cycling.**

Bars indicate mean iModulon activities  $\pm 95\%$  confidence interval. P-values are false discovery rate corrected p-values from a DiMA comparison of stressed transcriptomes (250 and/or 750  $\mu\text{M}$  PQ) between 0\_0 and evolved strains. **(A)** ArcA iModulon activities are mostly decreased after evolution, except in the case of mutations to arcAB ( $p = 0.035$ ). ArcA contains aerobic metabolism genes. **(B-D)** Fnr controls three iModulons with anaerobic metabolism genes, all of which are upregulated ( $p = 0.034, 0.030, 0.023$ ). **(E)** Knowledge graph describing changes in the evolved strains connecting central carbon mutations to anaerobic and glycolytic gene expression, which decreases TCA cycle flux and ROS generation. **(F)** The Cra iModulon, which contains glycolytic genes that are repressed by Cra, is upregulated ( $p = 0.017$ ). **(G)** The Crp-2 iModulon, which controls phosphotransferase systems, is upregulated ( $p = 0.022$ ). **(H)** The Pyruvate-2 iModulon is upregulated ( $p = 0.012$ ).

## KEY RESOURCES TABLE

REAGENT or RESOURCE	SOURCE	IDENTIFIER
<b>Bacterial and Virus Strains</b>		
Glucose Optimized <i>Escherichia coli</i> K12 MG1655	SBRG, University of California San Diego	PMID: 25304508 A4 F237 I1 R1
PQ Optimized <i>Escherichia coli</i> K12 MG1655 1_0	This paper	A16 F32 I1 R1
PQ Optimized <i>Escherichia coli</i> K12 MG1655 2_0	This Paper	A18 F36 I1 R1
PQ Optimized <i>Escherichia coli</i> K12 MG1655 3_0	This Paper	A14 F27 I1 R1
PQ Optimized <i>Escherichia coli</i> K12 MG1655 1_1	This Paper	A11 F83 I1 R1
PQ Optimized <i>Escherichia coli</i> K12 MG1655 1_2	This Paper	A13 F87 I1 R1
PQ Optimized <i>Escherichia coli</i> K12 MG1655 1_3	This Paper	A17 F104 I1 R1
PQ Optimized <i>Escherichia coli</i> K12 MG1655 1_4	This Paper	A19 F91 I1 R1
PQ Optimized <i>Escherichia coli</i> K12 MG1655 2_1	This Paper	A21 F97 I0 R1
PQ Optimized <i>Escherichia coli</i> K12 MG1655 2_2	This Paper	A25 F111 I1 R1
PQ Optimized <i>Escherichia coli</i> K12 MG1655 2_3	This Paper	A29 F119 I1 R1
PQ Optimized <i>Escherichia coli</i> K12 MG1655 3_1	This Paper	A1 F112 I1 R1
PQ Optimized <i>Escherichia coli</i> K12 MG1655 3_2	This Paper	A3 F76 I1 R1
PQ Optimized <i>Escherichia coli</i> K12 MG1655 3_3	This Paper	A7 F103 I1 R1
PQ Optimized <i>Escherichia coli</i> K12 MG1655 3_4	This Paper	A9 F77 I1 R1
<b>Chemicals, Peptides, and Recombinant Proteins</b>		
Paraquat Dichloride Hydrate	Sigma-Aldrich	36541–100MG
<b>Deposited Data</b>		
DNAseq	<a href="https://aledb.org">ALEdb.org</a>	ROS
RNAseq	NCBI GEO	GSE134256; GSE221314
PRECISE-1K iModulon Data	<a href="https://modulondb.org">iModulonDB.org</a> ; DOI: 10.1101/2021.04.08.439047	<i>E. coli</i> PRECISE-1K
<b>Oligonucleotides</b>		
Guide Sense Oligo Insert “T”: AGGCCAGCAAACAATGTAGcat	IDT	N/A
Guide Antisense Oligo Insert “T”: AAACatgCTACATTTGTTTGCTGG	IDT	N/A
Guide Sense Oligo Remove “T”: AGCGCAGCAAACAATGTAAGcat	IDT	N/A
Guide Antisense Oligo Remove “T”: AAACatgCTTACATTTGTTTGCTG	IDT	N/A
DONOR Forward Primer: CCAGGTCTCAGTGCCGACACAGCGCCTAT	IDT	N/A
DONOR Reverse Primer: CCAGGTCTCAGAGCCGTCGGCAGCATATGCA	IDT	N/A
<b>Software and Algorithms</b>		
iModulon Computation	DOI: 10.1101/2021.07.01.450581	<a href="https://github.com/avsastry/modulome-workflow">https://github.com/avsastry/modulome-workflow</a>
OxidizeME model	PMID: 31270234	<a href="https://github.com/SBRG/oxidizeme">https://github.com/SBRG/oxidizeme</a>
<b>Other</b>		



REAGENT or RESOURCE	SOURCE	IDENTIFIER
Code to generate all plots	This Paper	<a href="https://github.com/SBRG/ROS-ALE">https://github.com/SBRG/ROS-ALE</a>

Author Manuscript

Author Manuscript

Author Manuscript

Author Manuscript